JOURNAL OF THERMOPHYSICS AND HEAT TRANSFER
Vol. 18, No. 4, October–December 2004

Experimental and Theoretical Analysis of Enhanced Flat Miniature Heat Pipes

M. C. Zaghdoudi*
Institut National des Sciences Appliquées et de Technologie, 1080 Tunis, Tunisia
and
C. Tantolin† and C. Godet‡
Metal Process, 38800 Pont de Claix, France

A combined experimental and analytical study is realized to verify the miniature heat pipe (MHP) concept for cooling high-power dissipation electronic components and determine the potential advantages of constructing arrays of miniature channels as an integrated part of a heat pipe. A theoretical model is developed to predict the capillary limit and the thermal resistance of the flat MHP (FMHP). The model includes flow analysis and thermal study of the heat transfer modes in the capillary structures. To verify the mixed capillary structure concept and validate the proposed analytical model, an FMHP including a mixed capillary structure, rectangular grooves and screen wick, is manufactured, and a filling apparatus is developed charge such FMHPs. The heat transfer improvement obtained by comparing the heat pipe thermal resistance to the heat conduction thermal resistance of a copper plate having the same dimensions as the tested heat pipe is demonstrated for different heat input flux rates.

Nomenclature

A	=	cross sectional area, m^2
a	=	coefficient defined in Eqs. (33) and (45), $W/m^2 \cdot K^3$
B	=	bias contributor to the uncertainty due to instrument calibration
b	=	coefficient defined in Eqs. (33) and (45)
C_{wf}	=	wall/fluid coefficient defined in Eq. (42)
c_p	=	specific heat, $J/kg \cdot K$
D	=	dimensionless wire diameter
D_g	=	groove height, m
D_h	=	hydraulic diameter, m
d_s	=	wire diameter, m
F	=	friction coefficient, s/m^4
f	=	pressure losses factor
g	=	gravitational acceleration, m/s^2
I	=	current, A
K	=	permeability, m^{-2}
K_0	=	factor in Eq. (23)
L	=	flat miniature heat pipe (FMHP) overall length, m
La	=	Laplace constant, m
L_{eff}	=	FMHP effective length, m
N	=	mesh number, m^{-1}
N_g	=	number of grooves
N_s	=	number of screen layers
Nu	=	Nusselt number
P	=	contribution to the uncertainty due to equipment precision
Pr	=	Prandtl number
p	=	wetted perimeter, m
Q	=	heat transfer rate, W
Q_{evaps}	=	heat rate per unit volume transferred by evaporation within the screen mesh, W/m^3
Q_{max}	=	maximum capillary heat transfer rate, W
q	=	heat flux, W/m^2
q_{evaps}	=	heat flux transferred by evaporation within the screen mesh, W/m^2
q_{max}	=	maximum capillary heat flux, W/m^2
R	=	radius defined in Eq. (22), m
Re	=	Reynolds number
R_{th}	=	thermal resistance, K/W
r_c	=	capillary radius, m
r_{cc}	=	capillary radius at the condenser section, m
r_{ce}	=	capillary radius at the evaporator section, m
S	=	shrinkage coefficient
S_g	=	groove spacing, m
S_s	=	specific area, m^{-1}
T	=	temperature, °C
T_c	=	condenser temperature, °C
T_{ev}	=	evaporator temperature, °C
t	=	thickness, m
t_n	=	thickness of several screen layers, m
U	=	uncertainty
V	=	voltage, V
W	=	FMHP width, m
W_g	=	groove width, m
W_s	=	mesh aperture, m
W_v	=	overall width of the grooves, m
x, z	=	coordinate, m
Z	=	coefficient defined in Eq. (24)
α	=	dip at the contact point defined in Fig. 4c, deg
α^*	=	dimensionless length in Eq. (8)
β	=	factor defined in Eq. (18)
Δh_v	=	latent heat, J/kg
ΔP_c	=	capillary pressure, N/m^2
ΔP_l, ΔP_v, ΔP_g	=	liquid, vapor, and hydrostatic pressure drop, N/m^2
ΔT_{FMHP}	=	evaporator/condenser temperature difference, $T_{ev} - T_c$, °C
Θ	=	$T - T_{sat}$, °C
θ	=	angle defined in Fig. 3e, deg

Received 27 November 2002; accepted for publication 6 April 2004.

*Assistant Professor, Department of Physics and Instrumentation Institute of Applied Sciences and Technology, Centre Urbain Nord, BP Number 676; chaker.zaghdoudi@insat.rnu.tn. Member AIAA.

†Research and Development Engineer, Advanced Heat Transfer and Technology Division, 16 Rue Aristide Bergès, Z. I. des Iles; ahtt@metal-process.com.

‡Director, Advanced Heat Transfer and Technology Division, 16 Rue Aristide Bergès, Z. I. des Iles; ahtt@metal-process.com.

θ_c = contact angle at the condenser section, deg
θ_e = contact angle at the evaporator section, deg
λ = thermal conductivity, W/m · K
μ = dynamic viscosity, kg/m · s
ρ = density, kg/m^3
σ = surface tension, N/m
φ = porosity
φ_c = corner half-aperture angle, deg
ψ = tilt angle, deg

Subscripts and Superscripts

a = adiabatic
c = condenser, corner, capillary
ev = evaporator
evap = evaporation
eff = effective
g = groove, hydrostatic
l = liquid
max = maximum
min = minimum
s = screen
sat = saturation
v = vapor
w = wall

Introduction

RAPID growth in the use of internet and telecommunication services has created critical demands on the power required to energize this network. High-speed access coupled with expanding needs for all modes of electronic communications have resulted in telecommunications systems that exhibit dramatic increases in power dissipation compared to previous systems. Thermal management of electronic components must, therefore, solve problems connected with the limitations on the maximum chip temperature with the requirements of the level of temperature uniformity.

To cool electronic components, one can use air and liquid coolers, as well as coolers constructed on the principle of the phase change heat transfer in closed space, that is, immersion, thermosyphon, and heat pipe coolers. Each of these methods has its merits and drawbacks because in the choice of appropriate cooling one must take into consideration not only the thermal parameters of the cooler, but also design and stability of the system, durability, technology, price, application, etc.

Heat pipes are not in general a low-cost solution to the cooling problem, but are most effective and have great potential as power levels and volume requirements increase. For these reasons, heat pipes have been applied up to now mainly in application with special working conditions and requirements such as in space thermal control, in aircraft devices,[1] in traction drives,[2] in audio amplifiers, in cooling of closed cabinets in harsh environmental conditions, and so forth.

The present study deals with the development of an enhanced heat pipe concept to be used for cooling high-power dissipation electronic cards. Experiments are carried out to determine the potential advantages of constructing flat miniature heat pipes (FMHP) including a combined capillary structure, miniature-channel arrays, and screen wick. An analytical model is developed to identify and better understand the phenomena that govern the performance, limitations, and operating characteristics of such FMHPs.

Literature Survey on FMHP Experiments

We will focus on experimental studies dealing only with axially grooved FMHPs. The pulsating heat pipes are not considered in this study because the capillary mechanisms in such FMHPs are different from those of the grooved ones.

Murakami et al.[3] investigated the heat transport capability of two prototypes of flat miniature heat pipes with triangular (FMHP 1) and rectangular (FMHP 2) cross sections. Two working fluids are considered: methanol and ammonia. For the triangular cross section FMHP, the maximum capillary limits are $Q_{\max} = 1$ W and $Q_{\max} = 2$ W for methanol and ammonia, respectively. For the rectangular cross section FMHP, the maximum capillary limit is $Q_{\max} = 25$ W, which is obtained with methanol for the horizontal position.

Plesh et al.[4] tested two types of FMHPs (FMHP 1 and FMHP 2). FMHP 1 has two arteries, which are formed by the spars of an inserted frame and the wall of the casing. Transverse grooves are provided to allow transverse transport of liquid in the heating and cooling zones. FMHP 2, however, has longitudinal grooves over its entire length. For the first type, a maximum heat transfer rate of about 16.5 W is obtained in a horizontal position with a cooling water at 67°C. For the second type, the maximum heat transfer rate obtained is nearly $Q_{\max} = 70$ W, which corresponds to a heat flux of about $q_{\max} = 35$ W/cm^2 in a horizontal position with a cooling water temperature of 42°C. The temperature drop over the heat pipe is about $\Delta T_{\text{FMHP}} = 35$°C. For the thermosyphon position, the heat transfer capacity is even higher, where the maximum heat flux reaches $q_{\max} = 60$ W/cm^2.

Sun and Wang[5] developed and tested an aluminum FMHP. The inner surface of the heat pipe consists of 172 longitudinal V-shaped grooves. Three different working fluids are used: acetone (FMHP 1), ethanol (FMHP 2), and methanol (FMHP 3). For the aluminum/acetone FMHP, the maximum capillary limit is found to be about $Q_{\max} = 20$ W. The FMHP is not effective for low-power input (< 5 W) because it performs no better than a solid aluminum plate. The FMHPs are very sensitive to gravity. Acetone has been proven to be compatible with aluminum, whereas methanol and ethanol have been shown to be incompatible with aluminum.

Ogushi and Yamanaka[6] studied experimentally and theoretically the heat transport capability of flat heat pipes with rectangular and trapezoidal grooves. The topside wall of the heat pipe is made of a grooved brass plate, and the bottom wall is made of glass for visual inspection. The heat transfer performances of six types of rectangular grooves and three types of triangular grooves are obtained as a function of the heat pipe tilt and reversal of heat pipe configuration. The working fluid is methanol. It is found that the heat transport capability of triangular grooves varies with the orientation of the groove openings, upward or downward, whereas that of the rectangular grooves does not. Nucleate boiling is also observed in the rectangular grooves, and the heat transport capability is not found to be affected by nucleate boiling.

Cao et al.[7] tested two flat copper–water axially grooved miniature heat pipes that are fabricated by employing the electric discharge-machining (EDM) wire-cutting method. The two FMHPs are tested under different heat inputs, cooling temperatures, and orientations. The maximum heat transfer rate for the heat pipe tested is about $Q_{\max} = 40$ W, and the maximum heat flux achieved is about $q_{\max} = 20$ W/cm^2. The effective thermal conductance of the heat pipe is on the order of 40 times that of copper based on the external cross-sectional area of the miniature heat pipe.

Hopkins et al.[8] tested two copper–water FMHPs with diagonal trapezoidal microcapillary grooves at a slight angle to the heat pipes longitudinal axis (FMHP 1 and FMHP 2) and one copper–water FMHP (FMHP 3) with axial rectangular microcapillary grooves. FMHPs 1 and 2 are manufactured by a rolling method, and FMHP 3 is manufactured by a high-speed dicing saw employing a circular carbon steel blade with high diamond content. The FMHPs thermal performances depend on the orientation (horizontal wide, horizontal thin, and vertical positions), the heating method (one side heating or both side heating), and the operating temperature T_v. For the horizontal position and for $T_v = 90$°C, when the heat load is applied to both sides, $Q_{\max} = 8$ W ($q_{\max} = 11.4$ W/cm^2) for FMHP 1, whereas FMHP 2 exhibits a maximum heat flow rate of 20 W ($q_{\max} = 28.6$ W/cm^2). The maximum heat flow rate for FMHP 3 is found to be 128 W ($q_{\max} = 183$ W/cm^2). For the vertical position and for $T_v = 90$°C, FMHP 1 and FMHP 2 dissipate up to 78 and 88 W, respectively; however, FMHP 3 allows for $Q_{\max} = 164$ W. When one side of the FMHP is heated, the thermal performances are better than those obtained with both sides heated. Indeed, the maximum heat flux transferred by FMHP 1 is $q_{\max} = 38$ W/cm^2 for horizontal wide position and $q_{\max} = 114$ W/cm^2 for the vertical position ($T_v = 95$°C). For FMHP 2, $q_{\max} = 40$ W/cm^2 for the horizontal wide position and $q_{\max} = 112$ W/cm^2 for the vertical position. For FMHP 3, and for the horizontal position, $q_{\max} = 132$ W/cm^2 when the top side is heated and $q_{\max} = 156$ W/cm^2 when the bottom side is heated. For the vertical position, the maximum heat flux

transport capacity that FMHP 3 can dissipate is $q_{max} = 140$ W/cm^2. The authors conclude that FMHP 3 dissipated the highest heat flux in all orientations. It is also concluded that FMHPs with deep and narrow axial capillary grooves and thicker walls are much more promising than FMHPs with shallower trapezoidal grooves and thin walls. The majority of the experimental data show that the controlling mechanism of the maximum uniform heat flux at the evaporator is the capillary limitation. However, especially in the vertical orientation, the maximum heat load applied to FMHP 2 and FMHP 3 is restricted by the boiling limitation at higher operating temperatures.

Shimura et al.[9] developed aluminum FMHPs, which consist of aluminum containers, aluminum wire wicks, and R-123 as working fluid. The thermal performances of the FMHPs are determined according to the bending type, the inclination, and the heat input. The FMHPs are bent according to a step shape (the evaporator section being below the condenser section). Depending on the step height, five different FMHPs types are tested. It is found that the larger is the height of the step, the smallest ΔT_{FMHP} is, whatever the inclination. From life test result, it is found that long time reliability is confirmed, that is, R-123 is compatible to aluminum if R-123 contains less than 50 ppm concentration in water.

Schneider et al.[10–12] tested different structures of FMHPs: 1) FMHP 1, triangular grooves only; 2) FMHP 2, triangular grooves covered with one layer of screen wick; 3) FMHP 3, triangular grooves with screen wick-covered walls; and 4) FMHP 4, screen wicks only. The tests, which are carried out on FMHP 1, show that the heat is almost completely transported by conduction and not by transport of latent heat. Accordingly, the obtained thermal resistance is roughly the same as that of the solid material. When one screen wick layer is added on top of the groove structure (FMHP 2), the performance is only slightly increased. When one or two screens wick layers are pressed into the grooves (FMHP 3), the FMHP thermal performances are significantly enhanced. Heat transport capabilities of over 20 (FMHP 2) and 30 W (FMHP 3) are measured. The maximum capillary limit of FMHP 4 (box-type screen wick) is $Q_{max} = 25$ W.

Zampino and Kinzy Jones[13] fabricated and tested FMHPs that are compatible with high- and low-temperature ceramic multichip module (MCM-C) processing. The FMHPs are fabricated as an integral part of the MCM-C substrate using conventional numerically controlled machining operations. The FMHPs use an axially grooved wick structure, and the working fluid is water. Testing is performed using the heat pipe as a thermal spreader to enhance cooling by convection and for axial transport of heat to the edge of the substrate for cooling by conduction. Up to 16 W of heat are transported by the heat pipe with cooling provided along the condenser region by natural convection or by a temperature-controlled cooling jacket. In all cases, the temperature variation along the length of the substrate surface is less than 5°C. When a cooling jacket is used, the mean temperature along the substrate surface is less than 5°C above the cooling jacket temperature.

Wang and Vafai[14] reported on an experimental investigation of an asymmetrical flat plate heat pipe with geometrical dimensions presented in Table 1. The wicks are sintered copper powder, which covers the inner surfaces of the heat pipe wall, and the vapor region is composed of four identical channels. The results indicate that such FMHPs allow for heat fluxes up to 0.18 W/cm^2 ($Q_{max} = 12.8$ W) with a maximum evaporator/condenser temperature difference of about 2°C when the heat pipe is positioned vertically. (The heat source is located on the center of the FMHP.)

Zaghdoudi and Sarno[1] reported on the effects of body forces environment, gravitation, vibration, and acceleration forces, using constant heat load on the thermal performance of a flat copper–water heat pipe. The effect of gravitation forces is studied by testing the heat pipe in different positions: horizontal, antigravity, and thermosyphon. The experimental results on the orientation effects show that the heat pipe is hardly affected by the gravitation forces and exhibits nearly the same thermal performance whatever the tilt angle for input heat powers lower than 20 W. For input heat powers higher than 20 W, there is a slight heat pipe thermal performance dependency on gravitation.

Wang et al.[15] tested flexible FMHPs, which are fabricated by sintering an array of aluminum wires between two thin aluminum sheets. Three prototypes are fabricated. They differ from each other by the diameter of the wires and their number. The experimental results indicate that the flexible FMHPs have an effective thermal conductivity of more than 20 times that of the uncharged version and 10 times that of a solid material. This results in more uniform temperature distribution.

Cao and Gao[16] developed a new FMHP concept employing the boiling heat transfer mechanism in a narrow space. Two flat plate wickless network heat pipes (thermal spreaders) are designed, fabricated, and tested based on this concept. The fabricated thermal spreaders, which are made of copper or aluminum, are wickless, cross-grooved heat transfer devices that spread a concentrated heat source to a much large area. The network heat pipes are tested under different working conditions and orientations relative to the gravity, with water and methanol as working fluids. The maximum heat fluxes achieved are about 40 W/cm^2 for the methanol-filled heat pipe and 110 W/cm^2 for the water-filled one, corresponding to a total heat input of 393 W.

Ponnappan[17] investigated a folded screen-wick, copper–water FMHP. The wick is formed out of a commercially available mesh copper screen cloth. A rectangular-shaped wavy pattern with constant pitch is formed using a special fin-making process. Two porous stiffeners are inserted into the wick grooves for maintaining proper wick contact with the rectangular tube wall. Two modes of heating are used. Mode A uses one heater chip in the middle of the bottom surface of the FMHP. Mode B uses six heater chips. In the case of mode A heating ($T_v = 90$°C), the highest value of heat flux $q_{max} = 116$ W/cm^2 at the heater surface occurs at $Q_{max} = 90$ W. In the case of heating mode B ($T_v = 90$°C), the highest value of heat flux $q_{max} = 32$ W/cm^2 occurs at $Q_{max} = 150$ W.

Lin et al.[18] developed a high-performance miniature heat pipes for the cooling of high heat flux electronics using new capillary structures made of a folded copper sheet fin. The folded sheet fin is composed of capillary flow channels with fully and partially opened grooves, which are made by the EDM technique. Heat pipes with two different capillary structures and different fill amounts are tested in the horizontal position. Three heating modes of the evaporator are tested by activating different numbers of chip resistors. The heat pipe with partially opened groove wick performs better than that with fully opened groove wick. The condenser heat transfer coefficient is higher by 120% or more in the case of the former wick type compared to the latter at operating temperature of 110°C. Heat fluxes higher than 140 W/cm^2 are achieved using concentrated heating modes.

Wang and Peterson[19] developed and studied experimentally FMHPs utilizing arrays of parallel metal wires sandwiched between two thin metal sheets. The experimental results indicate that the maximum heat transport capacity increases with increases in wire diameter and that the overall value is proportional to the square of the wire diameter. These FMHPs allow for heat flux rates up to 30 W, which corresponds to heat fluxes less than 1 W/cm^2.

Table 1 lists the main geometrical characteristics of the FMHPs developed in the cited references. Table 2 gives the characteristics of the FMHP capillary structures. In Table 3 are listed the maximum heat fluxes obtained with the FMHPs. It can be seen from this overview that five types of FMHPs are developed:

1) Type 1 consists of FMHPs with only axial rectangular, triangular, or trapezoidal grooves.[3–8,13,18] These FMHPs allow for high heat fluxes for horizontal or thermosyphon positions (up to 150 W/cm^2). However, in the majority of the cases, the thermal performances of such FMHPs do not meet the electronic cooling requirements when the antigravity position is requested in as much as the FMHP thermal performances are greatly altered for these conditions because the standard capillary grooves are not able to allow for the necessary capillary pumping able to overcome the pressure losses.

2) Type 2 consists of FMHPs with mixed capillary structures, such as grooves and sintered metal powder or grooves and screen

Table 1 Overview of experimental studies of characteristics of FMHPs

Author reference	Overall dimensions, mm L	W	t	Evaporator $L_e \times l_e$	Condenser $L_c \times l_c$	Capillary structure	Material/fluid
Murakami et al.[3]	460	50	2.0	50 × 50 MHP end[a]	150 × 50 MHP end	Rectangular grooves (1) Triangular grooves (2) (2 prototypes)	Brass–glass–methanol
Plesh et al.[4]	120	7.0	2.0	——[b]	——[b]	Transverse grooves (1) Longitudinal grooves (2) (2 prototypes)	Copper–water
Sun and Wang[5]	286	45	4.0	45 × 45 Centered[c]	113 × 45 Dual[d]	V-shaped grooves (3 prototypes)	Aluminum–acetone–Ethanol–methanol
Ogushi and Yamanaka[6]	560	100	60	100 × 100 MHP end[a]	200 × 100 MHP end[a]	Rectangular–trapezoidal grooves (9 prototypes)	Brass–glass–methanol
Cao et al.[7]	82	7.0	2.8	19 × 7.0	20 × 7.0	Rectangular grooves (1)	Copper–water
	80	7.0	2.0	10 × 7.0 MHP end[a]	10 × 7.0 MHP end[a]	Rectangular grooves (2) (2 prototypes)	
Hopkins et al.[8]	120	7.0	2.0	15.6	34.4	Trapezoidal grooves (1)	Copper–water
	100	11.7	2.4	9.6	34.4	Trapezoidal grooves (2)	
	120.6	13.4	8.9	15.6 MHP end[a]	34.4 MHP end[a]	Rectangular grooves (3) (3 prototypes)	
Shimura et al.[9]	360 to 440	60	1.9	120 × 60 MHP end[a]	120 × 60 MHP end[a]	Aluminum wire wicks (5 prototypes)	Aluminum–R-123
Schneider et al.[10–12]	110	40	1.5	Ø20 MHP end[a]	Ø20 MHP end[a]	Triangular grooves and screen meshes (4 prototypes)	Metal matrix composite–water
Zampino and Kinzy Jones[13]	89	13	2.9	25 × 12 MHP end[a]	——[b]	Rectangular grooves (2 prototypes)	Cofire ceramic–water
Wang and Vafai[14]	190.5	139.7	34.9	139.7 × 50.8 Centered[c]	139.7 × 69.8 Dual[d]	Four channels and sintered copper powder (1 prototype)	Copper–water
Zaghdoudi and Sarno[1]	125	40	2.4	15 × 40 MHP end[a]	15 × 40 MHP end[a]	Rectangular grooves and sintered copper powder (1 prototype)	Copper–water
Wang et al.[15]	152	152.4	0.4	25.4 × 152.4 MHP end[a]	——[b]	Wires (1 prototype)	Aluminum–acetone
Cao and Gao[16]	200	200	4.6	9.86 × 37.5 Centered[c]	Remaining area acts as a condenser	Network of crossed grooves(1)	Aluminum–water Aluminum–methanol
	200	200	7	9.86 × 37.5 Centered		Network of axial triangular grooves (2) (2 prototypes)	Copper–water
Ponnappan[17]	107.9	10.2	3.9	18.5 × 10.2	32.5 × 10.2	Folded screen mesh (1 prototype)	Copper–water
Lin et al.[18]	108	12.7	6.35	18.5 × 12.55 MHP end[a]	32.5 × 12.55 MHP end[a]	Folded copper sheet fin (1)	Copper–water
	108	12.7	6.35	18.5 × 12.7 MHP end[a]	32.5 × 12.7 MHP end[a]	Notched folded sheet fin (2) (2 prototypes)	
Wang and Peterson[19]	152.4	152.4	0.4	25.4 × 152.4	34 × 240	Wire bonded (6 prototypes)	Aluminum–acetone

[a]Heat source is placed at one end of the FMHP. [b]Not specified in the reference. [c]Heat source is located at the FMHP center. [d]Both ends of the FMHP serve as condenser sections.

meshes.[1,10–12,14] Depending on the characteristics of the capillary structures, such as the pore diameter, the wire diameter, the wire spacing and the number for screen wick layers, these FMHPs could meet the electronic cooling requirements, especially for those applications where the electronic devices are submitted to forces such as gravity, acceleration, and vibration forces.[1] However, for standard applications, these FMHPs allow for low thermal performances (lower heat fluxes and higher thermal resistance) when compared to those delivered by the FMHPs of type 1.

3) Type 3 consists of FMHPs with groove-shaped screen wick.[17] These FMHPs allow for the same thermal performances as the axial grooved FMHPs. However, their fabrication process is easier because it does not include the machining of the grooves. Indeed, the wick is formed out of a metal wire cloth that is pressed into a square- or rectangle-shaped wavy or corrugated pattern with constant pitch by using a special industrial fin-making process. The main drawback of this technology is that the width of the screen needed to create a certain length, the screen thickness, the groove width, and the associated pitch of the fold/groove required are subject to the limitations of the fin machine and tooling.

4) Type 4 consists of FMHPs with bounded wires.[9,15,19] These FMHPs utilize an array of aluminum wires sintered or brazed between two thin aluminum sheets. The sharp corners formed between the wire and the case material are used as liquid arteries to pump the working fluid from the condenser to the evaporator section. In addition to providing capillary pumping, the solid wires are also useful in assisting in freeze prevention and recovery because of their ability to conduct heat axially and directly apply it to the liquid–vapor interface. In this design, the vapor flows through the microchannels formed between the individual wires.

5) Type 5 consists of wickless FMHPs.[16] These FMHPs utilize the concept of the boiling heat transfer mechanism in narrow space. These FMHPs can remove high heat flux rates with a large temperature gradient between the hot source and the cold one.

Table 2 Overview of experimental studies of capillary structures used within FMHPs

Reference	Capillary structures: Prototypes	Materials	Dimensions in mm	Charge	Weight
Murakami et al.[3]	MHP 1		Triangular grooves $D_g = 2$, $\theta_g = 30$ deg, $S_g = 3.2$		
	MHP 2	Brass	Rectangular grooves, $D_g = 0.4$, $W_g = 0.4$, $S_g = 0.8$	____[a]	____[a]
Plesh et al.[4]	MHP 1		Transverse grooves		
	MHP 2	Copper	Longitudinal grooves, no details given	____[a]	____[a]
Sun and Wang[5]	MHP 1	Aluminum	Triangular grooves, $W_g = 0.6$, $D_g = 0.4$, $S_g = 0$	4.1 ml Acetone	____[a]
Ogushi and Yamanaka[6]			Rectangular and trapezoïdal		
			N_g S_g W_g D_g W_g θ_g		
			Top *Bottom*		
	MHP 1		24 1.2 0.65 1.01 —— ——		
	MHP 2		14 2.0 1.01 1.06 —— ——		
	MHP 3	Brass	14 2.0 0.63 1.50 —— ——	____[a]	____[a]
	MHP 4		14 2.0 1.03 1.49 —— ——		
	MHP 5		14 2.0 0.64 0.52 —— ——		
	MHP 6		14 2.0 1.02 0.53 —— ——		
	MHP 7		14 2.0 1.28 1.88 0.23 15.6		
	MHP 8		14 2.0 1.83 1.94 0.21 22.6		
	MHP 9		11 2.5 2.44 2.02 0.08 30.3		
Cao et al.[7]			Rectangular		
			S_g W_g D_g		
	MHP 1	Copper	0.24 0.12 0.25	____[a]	____[a]
	MHP 2		0.20 0.10 0.25	____[a]	____[a]
Hopkins et al.[8]			Rectangular and trapezoïdal		
			N_g S_g W_g W_g D_g α_g		
			Top *Bottom*	(Water)	
	MHP 1	Copper	52 0.16 0.20 0.15 0.24 4	0.20 ml	____[a]
	MHP 2		50 0.20 0.45 0.30 0.20 18	20%	____[a]
	MHP 3		62 0.10 0.20 0.20 0.42 0	0.84 ml	____[a]
Shimura et al.[9]	5 MHPs	Aluminum	Wires, no details given	____[a]	____[a]
Schneider et al.[10–12]	4 MHPs	Copper	Triangular grooves and screen meshes, no details given	____[a]	____[a]
Zampino and Kinzy Jones[13]	2 MHPs	Cofire ceramic	Rectangular grooves, no details given	____[a]	____[a]
Wang and Vafai[14]	1 MHP	Copper	Four identical vapor channels, sintered copper powder		
			Thickness 1.651 mm, pore radius 3.1×10^{-5} m, porosity = 50%, permeability = 7×10^{-12}m^2	____[a]	____[a]
Zaghdoudi and Sarno[1]	1 MHP	Copper	Rectangular grooves and sintered powder $N_g = 35$, $W_g = 0.7$, $D_g = 0.9$, $S_g = 1.6$	1.4 ml (water)	75 grams
Wang et al.[15]			Wire bonded		
	MHP 1		$N_w = 43$ $D_w = 0.5$	____[a]	____[a]
	MHP 2	Aluminum	$N_w = 43$ $D_w = 0.8$		
	MHP 3		$N_w = 95$ $D_w = 0.5$		
Cao and Gao[16]	MHP 1	Aluminum	Perpendicular network of crossed grooves,	Water	
	MHP 2	Copper	$W_g = 2$, $D_g = 2$, $S_g = 4$	charging ratio	
			Triangular grooves, $W_g = 3$, $D_g = 3$, $S_g = 4$	≈ 0.6	____[a]
Ponnappan[17]	1 MHP	Copper	Folded screen wick, $N_g = 72$, $W_g = 0.2$, $D_g = 0.9$, $S_g = 0.31$	1.0 ml (water)	____[a]
Lin et al.[18]	MHP 1		Folded copper sheet fin,	0.87, 1.3 ml	
	MHP 2	Copper	$N_g = 32$, $W_g = 0.203$, $D_g = 0.89$, $S_g = 0.305$		
			Notched folded sheet fin, $N_g = 32$, $W_g = 0.203$, $D_g = 1.02$, $S_g = 0.305$	0.85, 1.3ml	____[a]
Wang and Peterson[19]			Wire bonded,		
	MHP 1		$N_w = 108$, $D_w = 0.33$, $S_w = 1.4$	____[a]	
	MHP 2		$N_w = 96$, $D_w = 0.406$, $S_w = 1.6$	____[a]	
	MHP 3	Aluminum	$N_w = 77$, $D_w = 0.635$, $S_w = 2.0$	1.8	____[a]
	MHP 4		$N_w = 84$, $D_w = 0.813$, $S_w = 1.8$	2.9	
	MHP 5		$N_w = 73$, $D_w = 1.016$, $S_w = 2.1$	4.3	
	MHP 6		$N_w = 59$, $D_w = 1.270$, $S_w = 2.6$	____[a]	

[a]Not specified in the reference.

Table 3 Maximum heat fluxes (W/cm^2)

Reference	FMHP prototype	Evaporator area, cm^{2c}	Orientation of FMHP		
			Horizontal	Thermosyphon	Antigravity
Murakami et al.[3]	MHP 1	25	<1	<1	——[a]
	MHP 2	25	<2	Up to 1.0	Up to 0.6
Plesh et al.[4]	MHP 1	——[a]	——[a]	——[a]	——[a]
	MHP 2	——[a]	Up to 35	Up to 60	——[a]
Sun and Wang[5]	MHP 1	20.25	Up to 0.5	——[a]	——[a]
	MHP 2	20.25	Up to 1.5	——[a]	——[a]
	MHP 3	20.25	Up to 1.0	——[a]	——[a]
Ogushi and Yamanaka[6]	MHP 2	100	<1.0	——[a]	——[a]
	MHP 3		<1.0	——[a]	——[a]
Cao et al.[7]	MHP 1	2.66	Up to 14	Up to 18	——[a]
	MHP 2	1.4	Up to 10	Up to 27	——[a]
Hopkins et al.[8]			Heating both sides		
	MHP 1	1.4	Up to 11	Up to 64	——[a]
	MHP 2	1.4	Up to 17	Up to 79	——[a]
	MHP 3	1.4	Up to 93	Up to 119	——[a]
			Heating one side		
	MHP 1	0.7	Up to 38	Up to 114	——[a]
	MHP 2	0.7	Up to 40	Up to 113	——[a]
	MHP 3	0.7	Up to 155	Up to 140	——[a]
Shimura et al.[9]	5 MHPs	72	<0.1	——[a]	——[a]
Schneider et al.[10–12]	MHP 1	3.141	Up to 11	——[a]	——[a]
	MHP 2	13.141	Up to 7	——[a]	——[a]
	MHP 3	13.141	Up to 14	——[a]	——[a]
	MHP 4	13.141	Up to 11	——[a]	——[a]
Zampino and Kinzy Jones[13]	MHP 1	3	Up to 6	——[a]	——[a]
Wang and Vafai[15]	1 MHP	71.0	<0.2	——[a]	——[a]
Zaghdoudi and Sarno[1]	1 MHP	6.0	Up to 10	10	10
Wang et al.[15]	1 MHP	——[b]	——[b]	——[a]	——[a]
Cao and Gao[16]	MHP 1	3.7	Up to 72	$\psi = 30$ deg, Up to 24.8	
	MHP 2	3.7	Up to 100	$\psi = 90$ deg, Up to 29.2	
				$\psi = 30$ deg, Up to 25.4	
				$\psi = 90$ deg, Up to 31.5	
Ponnappan[17]	1 MHP	1) 0.777	Up to 116	——[a]	——[a]
		2) 4.66	Up to 32	——[a]	——[a]
Lin et al.[18]	MHP 1	1) 0.774	158–283	——[a]	
		2) 1.548	80–157	——[a]	——[a]
		3) 4.644	Up to 32	——[a]	——[a]
	MHP 2	1) 0.774	158–283	——[a]	——[a]
		2) 0.774	80–157	——[a]	——[a]
		3) 4.644	Up to 28	——[a]	——[a]
Wang and Peterson[19]	MHP 3		Up to 0.3	——[a]	——[a]
	MHP 4	38.7	Up to 0.6	——[a]	——[a]
	MHP 5		0.77	——[a]	——[a]

[a]Not studied. [b]Not specified. [c]Calculated on the basis of the heater dimensions.

The present study will focus on FMHPs of type 2, especially those including a combined capillary structure: axial grooves and screen wicks. To study the effects of some parameters that could affect the thermal performance of such FMHPs, a prototype is developed and manufactured to determine their thermal performance and elaborate an analytical model able to predict the capillary limit and thermal resistance of these FMHPs in different operating conditions. Hence, a special focus on thermal modeling, fabrication, and charging procedures is presented in the following sections.

Theoretical Modeling of Mini Heat Pipe Thermal Performance

The objective is to develop a mathematical tool to predict the FMHP thermal performance and to be able to optimize the design of FMHPs, including composed wicks (rectangular grooves and screen meshes). The modeled FMHP has a rectangular cross section as shown in Fig. 1a. The inner wall of the heat pipe is covered by a screen wick type. It consists of a single or several layers of metal cloth. The geometrical characteristics of the screen mesh are listed in Table 4. The screen mesh is characterized by the number of pores per unit length N (mesh number), the wire diameter d_s, the wire mesh aperture W_s, and the number of the screen layers N_s. It can be an homogenous structure or a composite one that can include screens of different characteristics. Depending on the fluid fill charge, a part of the liquid can be present in the corners of the grooves. In that case, the corners will provide a supplementary capillary pumping to return the liquid back to the evaporator (Fig. 1b).

The liquid recedes into the corners of the grooves and into the mesh screen due to the evaporation. Near the evaporator end cap, the curvature radius of the liquid in the corners and in the mesh wick is very small. The minimum meniscus radius value is linked to the mesh screen geometry. In the condenser section, the wick is flooded with liquid. In case of an excessive fill charge, a liquid blocking occurs at the end of the condenser. The amount of liquid, hence, the interfacial radius of curvature, varies as a function of axial position z along the FMHP. The cross-sectional area of the liquid can be expressed in terms of geometrical dimensions, the contact angle of the meniscus θ, and the interfacial radius of curvature r_c.

Flow and Capillary Limit Analysis

For a heat pipe including composed wicks (grooves and screen meshes) to function properly, the net capillary pressure difference must be greater than the summation of all of the pressure losses occurring throughout the liquid and vapor flow. This relationship

Table 4 Main geometrical dimensions of the FMHP tested

Characteristics	Values
FMHP	
Width, W	35 mm
Length, L_t	125 mm
Thickness, t	3 mm
Evaporator length, L_e	15 mm
Condenser length, L_c	15–25 mm
Effective length, L_{eff}	110,105 mm
Inclination, ψ	−90, 0, +90 deg
Thermal conductivity, λ_w	380 W/m · K
Grooves	
Height, D_g	0.9 mm
Width, W_g	0.7 mm
Spacing, S_g	1.6 mm
Overall width of the grooves, W_v	30 mm
Number of grooves, N_g	19
Porosity, φ_g	0.44
Half-apex angle of the groove corner, φ_c	10 deg
Wetting angle, θ_e	35 deg
Screen meshes	
Wire diameter, d_s	0.05 mm
Mesh aperture, W_s	0.07 mm
Number of mesh screen layers, N_s	4
Mesh number, N	8333 m^{-1}(212/in.)
Porosity, φ_s	0.57
Thermal conductivity, λ_s	50 W/m · K

can be expressed as

$$\Delta P_c \geq \Delta P_v + \Delta P_l + \Delta P_g \tag{1}$$

where ΔP_c, ΔP_v, ΔP_l, and ΔP_g are the capillary pressure difference, the vapor pressure losses, the liquid pressure losses within the grooves and screen meshes, and the hydrostatic pressure, respectively.

To understand effectively the behavior of the vapor and liquid flow in an operating FMHP, each of the factors contributing to the overall pressure gradient must be clearly understood. The following paragraphs provide a detailed determination of each.

Capillary Pressure ΔP_c

The capillary pressure difference at the liquid–vapor interface can be found from the Laplace–Young equation. For many heat pipe wicking structures, the capillary pressure may be written in terms of a single radius of curvature, r_c, and the contact angle θ (Fig. 2a). When this is done, the capillary pressure difference between the evaporator and condenser sections can be expressed as

$$\Delta P_c = 2\sigma\cos(\theta_e)/r_{ce} - 2\sigma\cos(\theta_c)/r_{cc} \approx 2\sigma\cos(\theta_e)/r_{ce} \tag{2}$$

because it is generally assumed that the capillary radius in the condenser approaches infinity and $\theta_c = \pi/2$. For a screen-covered rectangular groove, the effective capillary radius r_{ce} is given by $(W_s + d_s)/2 = 1/(2N)$ (Fig. 2b). More recently, Noda and Kumagai[20] have investigated experimentally the maximum capillary pressure of a mesh screen, and from a correlation between the analytical and experimental results, a semi-empirical equation for predicting the maximum capillary pressure is developed. When the cross section of a meniscus is assumed to be bowed, the effect of the contact angle on the maximum capillary pressure can be expressed as

$$\Delta P_c = \frac{4\sigma\cos(\theta_e - \alpha)[0.106(\theta_e - \pi) + 0.5]}{(d_s + W_s) - d_s\cos\alpha} = \frac{4\sigma\cos(\theta_e - \alpha)}{(d_s + W_s)}\,\frac{[0.106(\theta_e - \pi) + 0.5]}{1 - D\cos\alpha} \tag{3}$$

where α is the dip at the contact point P (Fig. 2c) when the meniscus is just ruptured. The relationships between these parameters are

$$D = d_s/(d_s + W_s)$$

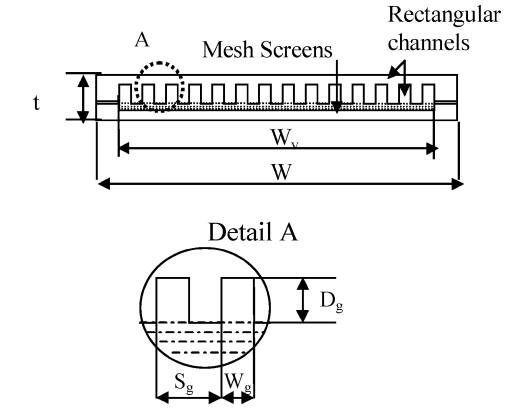

a) Cross section

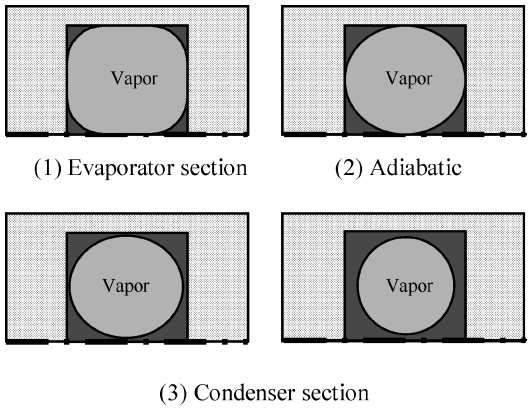

b) Operation principle

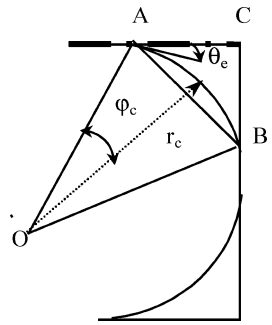

c) Geometrical characteristics of a corner

Fig. 1 FMHP developed in the present study.

$$\alpha = \begin{cases} \theta_e - \sin^{-1}\{D\sin\theta_e\}, & \text{if} \quad \theta_e < \tan^{-1}(-1/D) \\ \pi/2, & \text{if} \quad \theta_e \geq \tan^{-1}(-1/D) \end{cases} \tag{4}$$

The effect of the contact angle θ_e on the maximum capillary pressure ΔP_c is explained as follows: Because a mesh screen is formed by weaving vertical and horizontal wires having the same diameter d_s and the sieve opening W_s is larger than the wire diameter d_s, the maximum value of the dimensionless wire diameter D is 0.5 ($d_s = W_s$). As the dimensionless wire diameter D increases, the grid becomes smaller. Thus, when the contact angle θ_e is small, ΔP_c increases with increasing D. As θ_e increases, however, the dip α also increases, causing the dimensionless wire diameter D to have less effect. In the area where θ_e is large, the dip α is a constant $\pi/2$ and ΔP_c is a function of the contact angle θ_e only and ΔP_c is constant irrespective of the dimensionless wire diameter D.

Vapor Pressure Drop ΔP_v

The most widely accepted one-dimensional vapor pressure drop expression is the one presented by Chi[21]

$$\Delta P_v = (\mu_v/K_v N_g \bar{A}_v \rho_v \Delta h_v) L_{\text{eff}} Q \tag{5}$$

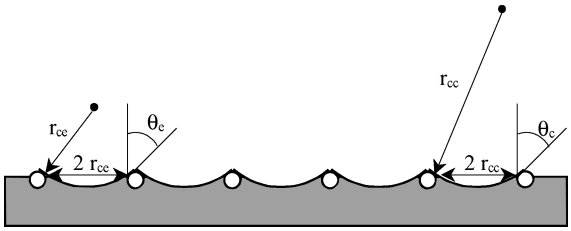

a) Capillary radii at the evaporator and condenser sections

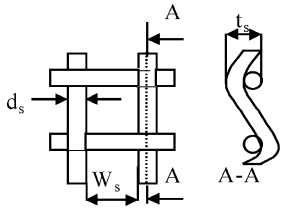

b) Screen mesh

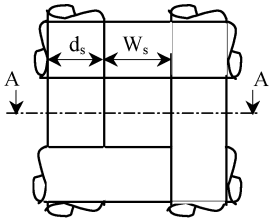

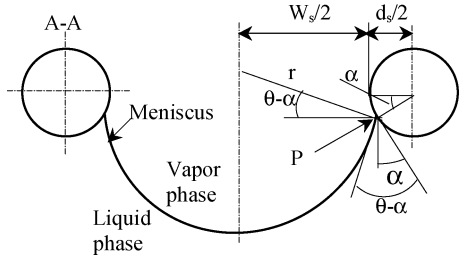

c) Liquid–vapor interface

d) Thickness of a screen mesh

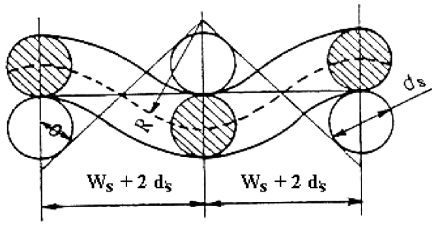

e) Shrinkage coefficient determination

Fig. 2 Geometrical parameters of the screen mesh.

L_{eff} is the effective length, which is given by $L_a + 0.5\ (L_{\text{ev}} + L_c)$ where L_a, L_{ev}, and L_c are the adiabatic, evaporator, and the condenser section lengths, respectively. K_v is the vapor permeability given by

$$K_v = D_{hv}^2 \big/ 2(f_v Re_v), \qquad \text{where} \qquad D_{hv} = 4\bar{A}_v/\bar{p}_v \tag{6}$$

D_{hv} is the hydraulic diameter of the vapor space. $\bar{A}_v$ and $\bar{p}_v$ are the mean values of the cross-sectional area and wetted perimeter of the vapor space in the grooves, respectively,

$$\bar{A}_v = N_g D_g W_g - \bar{A}_{lg}, \qquad \bar{p}_v = 2(D_g + W_g) - \bar{P}_{lg} \tag{7}$$

$\bar{A}_{lg}$ and $\bar{p}_{lg}$ are the mean values of the liquid cross-sectional area and wetted perimeter of the liquid in the grooves, respectively.

The velocity of the liquid phase is very small in comparison to that of the vapor flow, so that the interfacial shear for the vapor is computed by assuming the liquid to be stationary.[22] For a flat rectangular vapor channel configuration, the values of $(f_v Re_v)$ can be defined using the following equation[23]:

$$f_v Re_v = 24(1 - 1.355\alpha^* + 1.947\alpha^{*2} - 1.701\alpha^{*3} + 0.956\alpha^{*4} - 0.254\alpha^{*5}) \tag{8}$$

where $a^* = W_v/t_v$ when $W_v < t_v$ or $a^* = t_v/W_v$ when $W_v > t_v$. W_v and t_v are the width and the thickness of the vapor passage in the FMHP. In this study, these parameters are $W_v = N_g W_g$ and $t_v = D_g$.

Liquid Pressure Drop in the Grooves ΔP_{lg}

The liquid pressure drop is also the result of the combined effect of both viscous and inertial forces. For constant heat addition and removal, the liquid pressure drop in the grooves is

$$\Delta P_{lg} = (\mu_l / K_g N_g \bar{A}_{lg} \rho_l \Delta h_v) L_{\text{eff}} Q_g \tag{9}$$

where Q_g is the heat transfer rate dissipated in the grooves. A_{lg} and K_g are the liquid cross-sectional area and the permeability of the grooves, respectively. For a screen-covered rectangular groove, K_g is expressed as

$$K_g = \frac{D_{hlg}^2 \varphi_g}{2(f_l Re_l)} \qquad \text{where} \qquad D_{hlg} = \frac{4\bar{A}_{lg}}{\bar{P}_{lg}} \qquad \text{and} \qquad \varphi_g = \frac{W_g}{S_g} \tag{10}$$

D_{hlg} is the hydraulic diameter of the liquid in the grooves, and φ_g is the porosity of the groove.

The cross-sectional area and the wetted perimeter of the liquid depend on the curvature radius of the meniscus (Fig. 2b). In the expression of D_{hlg}, mean values of A_{lg} and P_{lg} are considered. These values are determined by integrating the local cross-sectional area and wetted perimeter along the FMHP, assuming a linear variation of the curvature radius between the value taken in the evaporator section, r_{ce} and that taken in the condenser section, r_{cc}. The value of the capillary radius in the evaporator section is assumed to be $r_{ce} = (W_s + d_s)/2 = 1/(2N)$ and that in the condenser section is $r_{cc} = D_{hv}/2$. When the schema of Fig. 2c, is considered, the following expressions of A_{lg} and P_{lg} can be written:

$$\bar{A}_{lg} = \frac{1}{L}\int_0^L A_{lg}(z)\,\mathrm{d}z = \frac{4}{3}\left[\sin^2\left(\frac{\pi}{4} - \theta_e\right) - \left(\frac{\pi}{4} - \theta_e\right) + \sin\left(\frac{\pi}{2} - 2\theta_e\right)\Big/2\right]\left(r_{ce}^2 + r_{cc}r_{ce} + r_{cc}^2\right) \tag{11}$$

$$\bar{P}_{lg} = \frac{1}{L}\int_0^L P_{lg}(z)\,\mathrm{d}z = 4\sqrt{2}\sin\left(\frac{\pi}{4} - \theta_e\right)(r_{ce} + r_{cc}) \tag{12}$$

For $f_l\ Re_l$, the relation from Schneider and DeVos[24] is used to take into account the shear stress in the liquid at the interface caused by the liquid–vapor frictional interaction. The same equation is used by Cao et al.,[7] Hopkins et al.,[8] and Khrustalev and Faghri.[25] Hence, for the case of a planar free-liquid surface geometry,

$$f_l Re_l = (f_l Re_l)_0 \left\{1 + \frac{N_g W_g^3}{6\pi D_{hlg}^3}(f_v Re_v)\frac{\mu_v}{\mu_l} \times \left[\frac{1}{3} - 1.971\exp\left(\frac{\pi D_g}{W_g}\right)\right]\right\} \tag{13}$$

where $(f_l Re_l)_0$ corresponds to the case of no liquid–vapor interaction, which can be evaluated using the following relation:

$$(f_l Re_l)_0 = 8\,D_g^2\left[\frac{W_g^2}{4}\left(1 + \frac{2D_g^2}{W_g}\right)^2\left(\frac{1}{3} - \frac{32W_g^2}{\pi^5 D_g}\tanh\frac{\pi D_g}{W_g}\right)\right]^{-1} \tag{14}$$

Liquid Pressure Drop in the Screen Mesh ΔP_{ls}

The liquid pressure drop in the screen mesh is given by

$$\Delta P_{ls} = (\mu_l / K_s A_s \rho_l \Delta h_v) L_{\text{eff}} Q_s \tag{15}$$

Q_s is the heat transfer rate dissipated in the screen meshes. A_s and K_s are the mesh screen cross-sectional area and the permeability, respectively. For a mesh screen, A_s and K_s are expressed as[26]

$$K_s = d_s^2 \varphi_s^3 \big/ 122(1-\varphi_s)^2, \qquad A_s = N_s(2d_s)W_v \tag{16}$$

N_s is the number of mesh screen layers and φ_s is the porosity of the mesh screen, which is given by Marcus's equation[27]

$$\varphi_s = 1 - \pi S N (d_s/4) \tag{17}$$

where S and N are the coefficient of shrinkage and the mesh number, respectively.

The relations for permeability [Eq. (16)] and porosity [Eq. (17)] do not take into consideration the effects of tightness and the number of wrapped screens. Ikeda[28] derived a model to take into account the number of screens. In the model proposed by Ikeda, the porosity is given by

$$\varphi_s = 1 - \pi N S d_s / 4(1+\beta) \tag{18}$$

where β is a factor that is the sum of the two others, β_0 and β_1. Here β_0 is the normalized clearance obtained from the measurement of the thickness with a layer of screen. It takes into the consideration that the thickness of a layer of metal woven screen is usually larger than twice that of the wire diameter. The reason for this is believed to be that, although the wires closely contact each other, the flatness of the woven screen is not perfect and the measurement is made with the screen cambered in such a condition as shown in Fig. 2d. The cambered screen can imaginably be flattened, displaying such an ideal reference condition (Fig. 2d) in which the wires closely contact each other and the woven screen is completely flat. In these conditions, β_0 is given by $\delta/2d_s$. Here β_1 takes into consideration that there is loose wrapping and imperfect installation of the screen wick. The following equation gives the normalized clearance β,

$$\beta = t_s / 2N_s d_s - 1 \tag{19}$$

where t_s is the mesh screen thickness.

For multiple layers of mesh screens, Kozai et al.[29] proposed an expression for porosity that takes into account the intermeshing between screen layers. The following relation for porosity can be used:

$$\varphi_{sn} = 1 - N_s t_s (1-\varphi_s)/t_n \tag{20}$$

where t_n is the thickness of the multiple layers and φ_s is the porosity of a single layer of screen. The porosity of a single layer is determined by measuring the displaced volume when the screen is submerged in a liquid. In the experiment conducted by Kozai et al.,[29] it is shown that the values of porosity predicted by Eq. (18) is 1–1.25 times larger than those predicted by Eq. (20).

The coefficient of shrinkage is determined on the basis of the geometric model for the shape of the woven wire as shown in Fig. 2e. Thus, the coefficient of shrinkage can be written as

$$S = 2R\theta/(W_s + 2d_s) \tag{21}$$

R and θ are the radius of curvature of the wire and the sector angle defined in Fig. 2e,

$$R\sin\theta = d_s/2, \qquad \tan(\theta/2) = d_s/(W_s + 2d_s) \tag{22}$$

On the basis of the experimental results for different screen meshes, Ikeda[28] proposed the following relation for the screen mesh permeability:

$$K_s = \varphi_s^3 d_s^2 \big/ 16 k_0 Z^2 S^2 (1-\varphi_s)^2 \tag{23}$$

Equation (23) takes the same form as the Blaque–Kozeney equation with the coefficient $16k_0Z^2S^2$ substituting for the numerical value of 122. The factor Z is a function of the wire diameter d_s, mesh number N, coefficient of shrinkage, and number of mesh screen layers N_s,

$$Z = 1 + 1/\pi d_s S N N_s \tag{24}$$

Because the porosity of the screen wick is affected by the normalized clearance and Z is affected by the number of layers, the permeability K_s will vary over a wide range. Here k_0 is assumed to be equal to 2, and the value of $32S^3Z^2$ is considered for the calculations.

Hydrostatic Pressure Drop

The axial hydrostatic pressure drop results from the component of the body force acting along the longitudinal axis,

$$\Delta P_g = \rho_l g L_{\text{eff}} \sin\psi \tag{25}$$

where ψ is the angle the heat pipe makes with respect to the horizontal.

Maximum Capillary Transferred Heat Rate

In a given cross section, the liquid pressure is the same in the grooves and within the screen mesh. This results in the same liquid pressure drop along the heat pipe in the grooves and within the screen mesh. The mass flow rates and the heat transfer rates transported by the grooves and by the screen mesh are dispatched to satisfy this condition. Equalizing Eqs. (9) and (15), rewritten in a simplified form, yields

$$\Delta P_l = \Delta P_{lg} = F_{lg} L_{\text{eff}} Q_g = \Delta P_{ls} = F_{ls} L_{\text{eff}} Q_s \tag{26}$$

where $F_{lg} = \mu_l/(K_g N_g A_g \rho_l \Delta h_v)$ and $F_{ls} = \mu_l (K_s A_s \rho_l \Delta h_v) \cdot Q_g$ and Q_s are the heat flow rates transferred within the grooves and the screens, respectively.

Considering that

$$\Delta P_l = F_l L_{\text{eff}} Q \tag{27}$$

where $Q = Q_g + Q_s$, we can deduce

$$F_l = [1/(1/F_{lg}) + (1/F_{ls})], \qquad Q_g = (F_l/F_{lg})Q$$
$$Q_s = (F_l/F_{ls})Q \tag{28a}$$

When Eq. (5) is rewritten by introducing the vapor coefficient factor F_v,

$$F_v = \mu_v / K_v N_g A_v \rho_v \Delta h_v \tag{28b}$$

the maximum capillary heat transfer rate can be deduced from Eqs. (26) and (28),

$$Q_{\max} = \frac{\Delta P_c \pm \Delta P_g}{(F_l + F_v) L_{\text{eff}}} \tag{29}$$

Heat Transfer Analysis

The overall miniature heat pipe thermal resistance R_{th} is expressed as

$$R_{\text{th}} = R_{\text{the}} + R_{\text{tha}} + R_{\text{thc}} \tag{30}$$

R_{the}, R_{tha}, and R_{thc} are the evaporator, adiabatic, and condenser thermal resistances, respectively. A detailed determination of each, based on a heat transfer analysis in both evaporator and condenser sections follows.

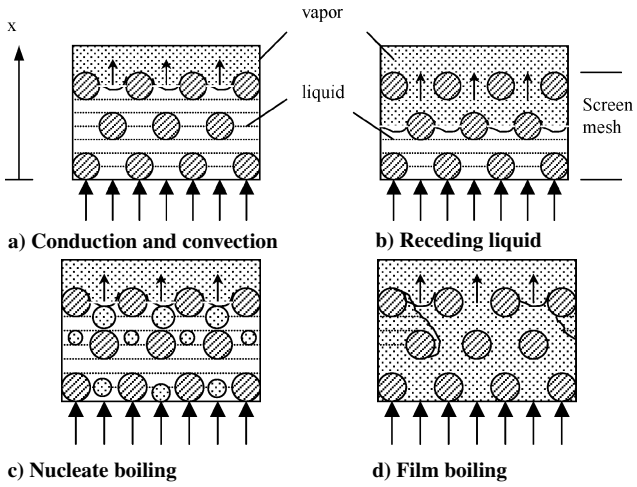

Fig. 3 Heat transfer mechanisms in screen mesh.

Heat Transfer in the Evaporator Section

Heat transfer in the screen mesh. Heat transfer from wicked surfaces is more complicated than that from plain surfaces due to the existence of capillary structures, and heat transfer and vapor formation may change with different types of wick structures. Three basic modes of heat transfer and vapor formation can be distinguished (Fig. 3).

First is conduction and convection: The wick is filled with liquid, and conduction occurs across the liquid layer and vaporization takes place from its surface (Fig. 3a). No boiling occurs within the wick. Thus, the heat transfer across the wick can be calculated by a conduction model. As the heat flux increases, the evaporation at the liquid surface is augmented (Fig. 3b). The capillary forces may not be sufficient to drive a sufficient amount of liquid back to the evaporator zone. As a result, the liquid layer begins to recede into the wick structure. If the receding of the liquid continues, the liquid at the evaporator may be completely depleted. This heat pipe limit that is encountered is actually the capillary limit. The heat transfer across the liquid layer is still by conduction, and the liquid vaporization takes place at the liquid–vapor interface.

The second mode is nucleate boiling (Fig. 3c): When the temperature difference across the wick is large, nucleate boiling may take place within the wick. This heat transfer mode represents a heat transfer limit for the following reasons: Large bubbles bursting at the liquid surface may disrupt the menisci established at the liquid–vapor interface and eliminate the capillary force circulating the liquid condensate; vapor bubbles generated at the evaporator section may block the liquid return from the condenser section.

The third mode is film boiling (Fig. 3d): A large number of bubbles are generated as the temperature difference across the wick is increased. These bubbles coalesce together before escaping to the surface, forming a layer of vapor adjacent to the heated wall, which prevents the liquid from reaching the wall surface. As a result, the heat pipe wall increases rapidly and the heat pipe may be burned out.

To determine the thermal resistance of the screen mesh when convection and evaporation modes are predominant (high heat fluxes), the following analysis is developed. In this analysis, it is assumed that the situation can be modeled as a steady one-dimensional problem, the properties of the wick are homogeneous, and the saturation temperature is constant throughout the wick. Also, the wick is assumed to be completely saturated and the wick is firmly bonded to itself and the wall. The conservation of energy equation for this situation is

$$\frac{\mathrm{d}^2T}{\mathrm{d}x^2} - \frac{\mathrm{Q}_{\mathrm{evaps}}}{\lambda_{\mathrm{seff}}} = 0 \tag{31}$$

where the effective thermal conductivity λ_{seff} of the mesh screen is given by

$$\lambda_{\mathrm{seff}} = \frac{\lambda_l[\lambda_l + \lambda_s - (1-\varphi_s)(\lambda_l - \lambda_s)]}{[\lambda_l + \lambda_s + (1-\varphi_s)(\lambda_l - \lambda_s)]} \tag{32}$$

Q_{evaps} is the heat source per unit volume, due to evaporation within the screen mesh, which can be expressed as

$$Q_{\mathrm{evaps}} = aS_s[T(x) - T_{\mathrm{sat}}]^b \tag{33}$$

where S_s is the specific surface area, which is the surface area per unit volume of the screen mesh. Combining Eqs. (31) and (33) yields

$$\frac{\mathrm{d}^2T}{\mathrm{d}x^2} - \frac{aS_s}{\lambda_{\mathrm{seff}}}[T(x) - T_{\mathrm{sat}}]^b = 0 \tag{34}$$

In this analysis, the wick structure is considered thick, the wick thermal conductivity is low because it is made of brass ($\lambda_s = 50$ W/m · K), and the specific surface area is large; the heat transfer through the mesh screen can be modeled as through a wick of semi-infinite thickness. The boundary conditions in this case are

$$\text{at } x = \infty : T = T_{\mathrm{sat}}, \qquad \frac{\mathrm{d}T}{\mathrm{d}x} = 0 \tag{35}$$

Equation (34) is solved with the temperature gradient boundary condition in Eq. (35) by using separating variables method and integrating across the thickness of the mesh screen. The expression of the wick temperature distribution is

$$\Theta(x) = \left[\left(\frac{b-1}{2}\right)\sqrt{\frac{2aS_s}{\lambda_{\mathrm{seff}}(b+1)}}x + \Theta_w^{(1-b)/2}\right]^{2/(1-b)} \tag{36}$$

where $\Theta(x) = T(x) - T_{\mathrm{sat}}$ and $\Theta_w = T_w - T_{\mathrm{sat}}$.

An energy balance between the input heat flux q_w, the heat flux transferred by evaporation within the screen mesh q_{evaps}, and the heat flux transferred by conduction through the screen mesh q_{cs} at the wall–wick interface ($x = 0$) yields

$$q_w = q_{\mathrm{evaps}} + q_{\mathrm{cs}} = \varphi_s a\Theta_w^b - \lambda_{\mathrm{seff}}\left.\frac{\mathrm{d}\Theta}{\mathrm{d}x}\right|_{x=0} \tag{37}$$

Substituting Eq. (36) into Eq. (37) gives

$$q_w = \varphi_s a\Theta_w^b + \frac{\sqrt{2a\lambda_{\mathrm{seff}}S_s}}{(b+1)}\Theta_w^{(b+1)/2} \tag{38}$$

The specific surface area S_s is given by

$$S_s = 4(1-\varphi_s)/d_s \tag{39}$$

The determination of $R_{\mathrm{th}se}$ needs a complete knowledge of a and b. For evaporative flow processes, Rohsenow and Clark[30] developed a model commonly used

$$Nu = (1/C_{\mathrm{wf}})Re^{(1-n)}Pr^{-m} \tag{40}$$

The Nusselt and Reynolds numbers are defined as follows:

$$Nu = \frac{q_{\mathrm{evaps}}La}{\Theta_w\lambda_l}, \qquad Re = \frac{q_{\mathrm{evaps}}La}{\mu_l\Delta h_v} \tag{41}$$

where the characteristic length in the Reynolds and the Nusselt numbers is the Laplace constant La,

$$La = \sqrt{\sigma/g(\rho_l - \rho_v)} \tag{42}$$

and q_{evap} is the heat flux transferred by evaporation within the wick, $q_{\mathrm{evap}} = Q_{\mathrm{evap}}/Ss$.

Rearranging Eq. (40) and comparing with Eq. (33) yields

$$q_{\mathrm{evaps}} = \left[1/C_{\mathrm{wf}}(La/\mu_l\Delta h_v)^{1-n}(\mu_l c_{pl}/\lambda_l)^{-m}\lambda_l/La\right]^{1/n}\Theta_w^{1/n} \tag{43}$$

Hence, a and b can be identified as

$$a = [1/C_{\mathrm{wf}}(La/\mu_l\Delta h_v)^{1-n}(\mu_l c_{pl}/\lambda_l)^{-m}\,\lambda_l/La]^{1/n}, \qquad b = 1/n \tag{44}$$

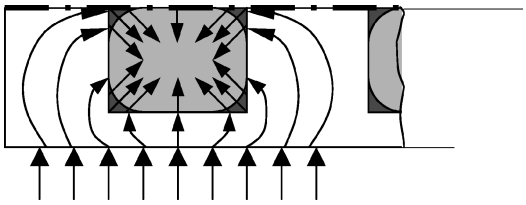

a) Evaporator section

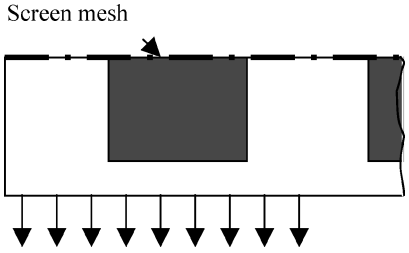

b) Condenser section

Fig. 4 Heat transfer mechanisms in groove.

For water–copper fluid–material combination, Rohsenow and Clark[30] suggested $C_{\mathrm{wf}} = 0.013$, $n = 1/3$, and $m = 0$. This results in the following values of a and b:

$$a = \frac{455{,}166}{La\lambda_l^{-3}\mu_l^2\Delta h_v^2}, \qquad b = 3 \tag{45}$$

The determination of the thermal resistance due to evaporation within the screen mesh is deduced from Eq. (38) by an iterative method. Indeed, when the value of q_w is known, which is calculated on the basis of the heat flux rate transferred through the screen mesh and the area of the evaporator section, the thermal resistance due to evaporation is calculated from

$$R_{\mathrm{th}sevap} = \Theta_w/Q, \qquad q_w = Q/(L_e W_v) \tag{46}$$

Heat transfer in the groove. In the groove, most of the liquid is evaporated at the thin liquid film region near the liquid–vapor interface–wall contact (Fig. 4a). This means that most of the heat bypasses the liquid in the corners of the groove. Heat is conducted through two parallel paths. The first path is through the liquid in the channel, and so the thermal conductivity is $\lambda_1 = \lambda_1$. The second path consists of two thermal resistances in series. The heat travel through the fin wall and then through the thin liquid film. Chi[21] stated that the film heat transfer coefficient at the fin–thin-film interface is $\lambda_1/[0.185(S_g - W_g)]$. Therefore, the conductivity of the second path is

$$\lambda_2 = \lambda_l\lambda_w D_g/[0.185(S_g - W_g)\lambda_w + D_g\lambda_1]$$

The effective thermal conductivity of the groove wick in the evaporator section is found by combining λ_1 and λ_2 in parallel,

$$\lambda_{g\mathrm{eff}e} = \frac{D_g(S_g - W_g)\lambda_w\lambda_l + (W_g\lambda_l)[0.185(S_g - W_g)\lambda_w + D_g\lambda_l]}{S_g[0.185(S_g - W_g)\lambda_w + D_g\lambda_l]} \tag{47}$$

Hence, the thermal resistance due to the evaporation within the groove is expressed as

$$R_{\mathrm{th}g\mathrm{evap}} = D_g/\lambda_{g\mathrm{eff}e}L_e W_v \tag{48}$$

The thermal resistance of the evaporator section is determined by considering two parallel paths of the heat. The first path is through the screen mesh, so that the thermal resistance is $R_{\mathrm{th}sevap}$. The second path is through the groove, and the corresponding thermal resistance is $R_{\mathrm{th}g\mathrm{evap}}$,

$$R_{\mathrm{th}e} = R_{\mathrm{th}w\mathrm{evap}} + \frac{R_{\mathrm{th}sevap}R_{\mathrm{th}g\mathrm{evap}}}{(R_{\mathrm{th}sevap} + R_{\mathrm{th}g\mathrm{evap}})} \tag{49}$$

where $R_{\mathrm{th}w\mathrm{evap}}$ is the thermal resistance due to conduction through the wall thickness of the heated side of the FMHP. This thermal resistance depends on the heating mode.

Heat Transfer in the Condenser Section

In the condenser, vapor is condensed over the entire liquid–vapor interface, as shown in Fig. 4b. For the groove, the heat is conducted through two separate paths, with the first path through the thin film and the fin, in series, and the second path only through the liquid in the groove. Hence, the effective thermal conductivity of a rectangular groove wick in the condenser section is (parallel heat conduction path)

$$\lambda_{g\mathrm{eff}c} = \varphi_g\lambda_l + (1-\varphi_g)\lambda_w \tag{50}$$

We have also to take into account conduction through the mesh screen, and with use of simple circuit analysis, the effective thermal conductivity of the groove-covered mesh screen in the condenser section is written as

$$\lambda_{\mathrm{eff}c} = \frac{(D_g + t_n)\lambda_{g\mathrm{eff}c}\lambda_{s\mathrm{eff}}}{(D_g\lambda_{s\mathrm{eff}} + t_n\lambda_{g\mathrm{eff}c})} \tag{51}$$

The condenser thermal resistance $R_{\mathrm{th}c}$ includes the thermal resistance $R_{\mathrm{th}wc}$ due to conduction through the FMHP wall and the thermal resistance due to the condensation through the grooves and the meshes,

$$R_{\mathrm{th}c} = \frac{t_w}{\lambda_w L_c W_v} + \frac{(D_g + t_n)}{\lambda_{\mathrm{eff}c}L_c W_v} \tag{52}$$

Heat Transfer in the Adiabatic Section

The adiabatic vapor resistance, although usually negligible, can be found as[31]

$$R_{\mathrm{th}a} = \frac{T_v(P_{ve} - P_{vc})}{\rho_v\Delta h_v Q} \tag{53}$$

where P_{ve} and P_{vc} are the vapor pressures at the evaporator and condenser sections, respectively.

Combining these individual resistances provides a method by which the overall thermal resistance can be computed, and hence, the temperature drop associated with various axial fluxes can be determined.

Numerical Treatment

The capillary limit $Q_{\max}$ and FMHP thermal resistance are determined according to the following procedure:

1) Introduce overall FMHP dimensions (Table 4) and determine all physical parameters.

2) Fix an arbitrary value of T_{sat} and calculate the fluid properties.

3) Calculate the liquid and vapor friction coefficients F_l and F_v [Eqs. (28a) and (28b)].

4) Calculate $Q_{\max}$ [Eq. (29)].

5) Calculate the thermal resistance at the evaporator section $R_{\mathrm{th}e}$ by an iterative method from Eqs. (48) or (49), depending on the heating method.

6) Calculate the thermal resistance of the condenser section $R_{\mathrm{th}c}$ from Eq. (52).

7) Calculate the thermal resistance of the adiabatic section $R_{\mathrm{th}a}$ from Eq. (53).

8) Calculate the FMHP thermal resistance from Eq. (30).

9) Determine the actual value of T_{sat} from the energy balance at the condenser section.

10) Steps 3–9 are repeated until convergence on the T_{sat} value. The convergence criterion is that the difference between the T_{sat} value issued from previous iteration and that calculated in current iteration is less than 10^{-3} °C.

FMHP Prototyping

FMHP Fabrication

The FMHP prototypes have been machined as shown in Fig. 1. The main geometrical dimensions of the miniature heat pipes are listed in Table 4. The FMHP is manufactured with an axial and rectangular capillary groove structure and mesh screens (Fig. 1). The heat pipe body is manufactured in two halves. Manufacturing of FMHP begins with the capillary grooves being mechanically machined in the first-half (1.5 mm thick). The second-half, which consists of a copper cover slip 1 mm thick including four mesh screens, is bonded to the first-half by an electron beam welding process. The heat pipe charging tube (2 mm diameter), from which the fluid working is introduced to the heat pipe, is bounded to the heat pipe end by a classic welding technique. The geometrical characteristics of the mesh screens are listed in Table 4.

Filling Procedure

Because the miniature heat pipe has a very small interior space, filling the heat pipe presents one of the greatest challenges. In this study, a boiling method is used for the filling purpose. The filling assembly is schematically shown in Fig. 5, which includes a vacuum system, a boiler filled with distilled water, vacuum tight electrovalves, a burette for a precise filling of the FMHP, and a tubular adapter. The degassing and charging procedure consists of the following steps: 1) degassing water by boiling process, 2) creating a vacuum in the complete setup, 3) charging of the burette, and 4) charging of the FMHP. An automatic process controls the steps in the following manner:

For step 1, degassing water by boiling process, all electrovalves (V_1–V_8) are closed, and water is heated to 120°C for 30 min. After that, electrovalve V_1 is opened, and air in vented to the atmosphere. To optimize this process, a finned tube, which is air cooled, is sealed in the top part of the boiler so that vapor can condense, and only noncondensable air is evacuated when the electrovalve is opened.

For step 2, evacuating the complete setup, first, $V_3 - V_6$ are opened, and V_8 is closed. Second, V_7 is closed if the vacuum pressure is under 10^{-3} mbar, and third, V_8 is opened till a minimum pressure up to 10^{-5} mbar is reached.

For step 3, charging the burette, first, V_6 and V_8 are closed; second, V_2 and V_3 are opened and V_4 is closed; and third, V_2 and V_3 are closed.

For step 4, charging the FMHP, V_4 and V_5 are opened.

In the fill charge procedure, excessive working fluid is needed because some liquid could stick to the inner walls of the hose and the tube adapter. After charging the FMHP, the open end (a 2-mm-diam charging tube) is sealed. The amount of liquid is controlled by weight in an accurate balance. Indeed, the FMHP is weighed before and after the fill charging process, and it is found that the optimum fill charge for the FMHP developed in this study is about 1.4 ml. To obtain good repeatability and reproducibility of the fill charge amounts, all hoses are heated to 100°C and the FMHP temperature is controlled and kept at 25°C, so that excessive condensation in the houses is avoided and the liquid is swept in the heat pipe and trapped by the condensation process.

Experimental Study

Experimental Setup and Procedure

Heat input is delivered by a 35 × 15 mm film resistor attached at one end of the FMHP, and it is provided on either the mesh screen side of the FMHP or the grooved side (Fig. 6a). Contact resistance

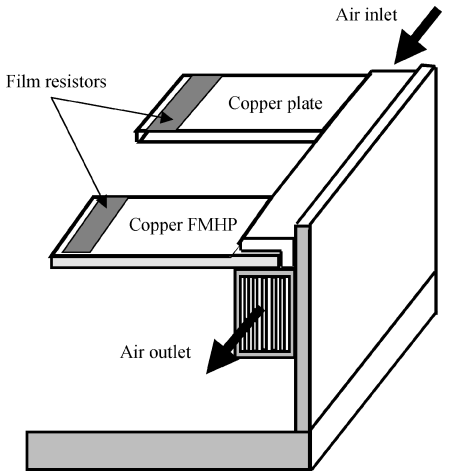

a) Test rig

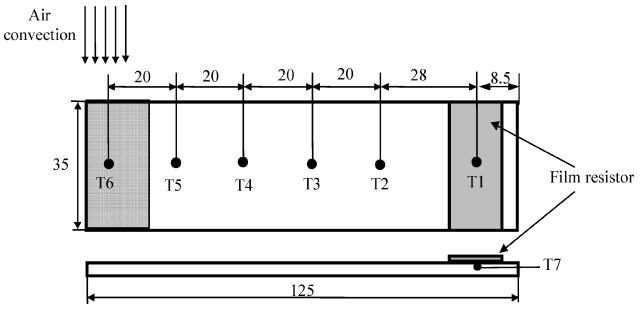

b) Thermocouple locations

Fig. 6 Experimental setup.

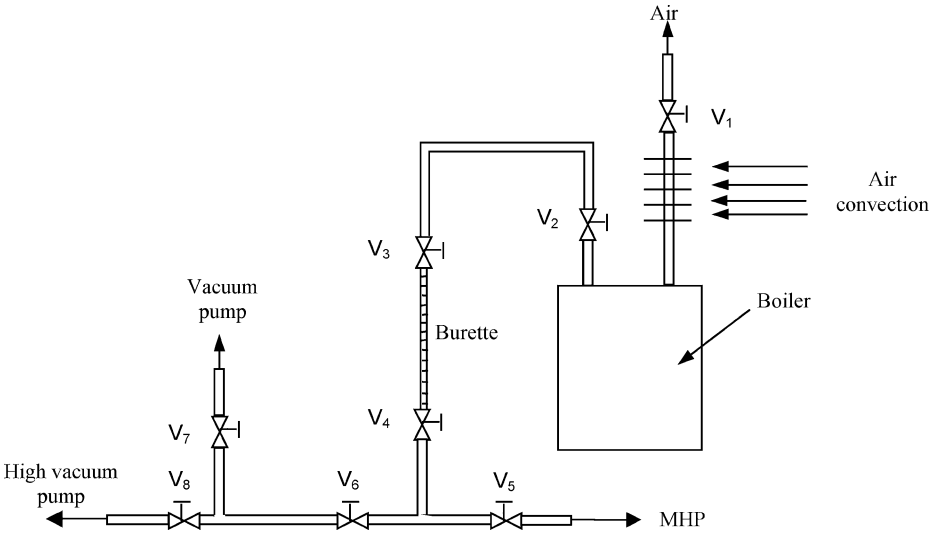

Fig. 5 Filling assembly.

at the resistor–wall interface is reduced by applying a 3M high thermal conductive interface material. A comparative technique is used to evaluate the steady-state and transient behaviors of the FMHPs. In this technique, the same experimental setup as considered for the FMHP is used for an ungrooved copper plate having the same dimensions as the FMHP. The two heaters (for the FMHP and the copper plate) are connected in parallel to ensure that a constant power is supplied to each heated section. The voltage and current are measured using digital voltmeter and ammeter. The power input is controlled by controlling the voltage with the variable transformer. Both the evaporator and the adiabatic sections are thermally insulated. The heat loss from the insulation surface to the ambient is determined by evaluating the temperature difference and the heat transfer coefficient of natural convection between the insulated outer surface and ambient. Heat losses to the environment of a functioning heat pipe are than closely approximated (less than 1%) vs operating temperature. Heat is removed from the FMHP by air convection (Fig. 6a). A thermally conductive paste is used to enhance the heat transfer between the copper FMHP and the aluminum blocks. The heat sink area can be varied so that FMHP thermal performance for different condenser lengths to be determined. The temperature distribution across the surface of the copper FMHP and the copper plate is obtained using seven type-J surface-mounted thermocouples. The thermocouples are located at 8.5, 36.5, 56.5, 76.5, 96.5, and 116.5 mm from the end cap of the evaporator section (Fig. 6b). To measure the evaporator and condenser temperatures, grooves are applied in the heater and the condenser locations and thermocouples are inserted along the grooves so that the thermocouples are in contact with the FMHP wall.

The experimental investigation focuses on the heat transfer characteristics of the FMHP with different positions at various heat rates Q and operating temperatures. Input power is varied in increments from a low value to the power at which the evaporator temperature starts to increase rapidly. In the process, the temperature distribution of the heat pipe along the longitudinal axis is observed and recorded. All experimental data are obtained with a systematic and consistent methodology that is as follows. First, the FMHP is positioned in the proper orientation and a small heat load is applied to the evaporator section by use of the film resistor. Second, the heat sink operating temperature is obtained and maintained by adjusting the airflow to the aluminum finned heat sink. Once the heat sink temperature is obtained, the system is allowed to reach steady state over 10–15 min. After steady state is reached, temperature readings at all thermocouples are recorded, and power to the evaporator is increased by a small increment. This cycle is repeated until the maximum capillary limit is reached, which is characterized by a sudden and steady rise of the evaporator temperature.

Measurement Uncertainty Analysis

The Siemens Multireg C1372 data acquisition system is used to make all temperature measurements. The type-J thermocouples are calibrated against a precision digital resistive temperature device (RTD) and the accuracy over the range of interest is found to be within 0.5°C. In the steady state, the wall thermocouples fluctuate within 0.2°C. The uncertainty of the thermocouples is $0.3^{\circ}\mathrm{C}+0.03.10^{-2}\ T$, where T is the measured temperature. The uncertainty of the thermocouples locations is within 0.5 mm in the heat pipe axial direction. A pair of multimeters are used to determine and record the power supplied to the resistors. The first multimeter is used to measure voltage across the film resistor and has an accuracy of 2% of true voltage, whereas the second measures the ac current and has an accuracy 2% of true ac current.

The power input to the electric heater is calculated using the measured current and voltage ($Q = V \times I$). The thermal resistance R_{th} of the heat pipe is defined as the ratio of the temperature drop, $\Delta T_{\mathrm{FMHP}} = T_{\mathrm{ev}} - T_c$, across the heat pipe to the input heat power Q. The uncertainty of the data is estimated by the method of Kline and McClintok.[32]

The 95% confidence uncertainty on the thermal resistance, $U_{R\mathrm{th}}$, in the experimental result of R_{th}, is given by the combination of a precision contribution to the uncertainty of R_{th}, $P_{R\mathrm{th}}$, and a bias contribution to the uncertainty of R_{th}, $B_{R\mathrm{th}}$,

$$U_{R\mathrm{th}} = \left[B_{R\mathrm{th}}^2 + P_{R\mathrm{th}}^2\right]^{\frac{1}{2}} \tag{54}$$

because the heat pipe thermal resistance R_{th} is calculated from

$$R_{\mathrm{th}} = \Delta T/Q = (T_{\mathrm{ev}} - T_{\mathrm{c}})/Q \tag{55}$$

The precision and bias limits contributions can be evaluated separately in terms of the sensitivity coefficients of the result, R_{th}, to the measured quantities following the propagation of Kline and McClintock[32]

$$P_{R\mathrm{th}}^2 = \left(\frac{\partial R_{\mathrm{th}}}{\partial T_{\mathrm{ev}}}\right)^2 P_{T\mathrm{ev}}^2 + \left(\frac{\partial R_{\mathrm{th}}}{\partial T_c}\right)^2 P_{Tc}^2 + \left(\frac{\partial R_{\mathrm{th}}}{\partial Q}\right)^2 P_Q^2 \tag{56}$$

$$B_{R\mathrm{th}}^2 = \left(\frac{\partial R_{\mathrm{th}}}{\partial \mathrm{T}_{\mathrm{ev}}}\right)^2 B_{T\mathrm{ev}}^2 + \left(\frac{\partial R_{\mathrm{th}}}{\partial T_c}\right)^2 B_{Tc}^2 + \left(\frac{\partial R_{\mathrm{th}}}{\partial Q}\right)^2 B_Q^2 + 2\left(\frac{\partial R_{\mathrm{th}}}{\partial T_{\mathrm{ev}}}\right)\left(\frac{\partial R_{\mathrm{th}}}{\partial T_c}\right) B'_{Tc} B'_{T\mathrm{ev}} \tag{57}$$

where B'_{Tc} and $B'_{T\mathrm{ev}}$ are the portions of B_{Tc} and $B_{T\mathrm{ev}}$ that arise from identical error sources (calibration errors of thermocouples that were calibrated using the same standards, equipment, and procedures) and are, therefore, presumed to be perfectly correlated.

Using Eq. (55) to evaluate the derivatives, defining, $\Delta T = T_{\mathrm{ev}} - T_c$, and rearranging, one obtains

$$(P_{R\mathrm{th}}/R_{\mathrm{th}})^2 = (P_{T\mathrm{ev}}/\Delta T)^2 + (P_{Tc}/\Delta T)^2 + (P_Q/Q)^2 \tag{58}$$

$$(B_{R\mathrm{th}}/R_{\mathrm{th}})^2 = (B_{T\mathrm{ev}}/\Delta T)^2 + (B_{Tc}/\Delta T)^2 + (B_Q/Q)^2 - 2(B'_{T\mathrm{ev}}/\Delta T)(B'_{Tc}/\Delta T) \tag{59}$$

where

$$(P_Q/Q)^2 = (P_V/V)^2 + (P_I/I)^2 \tag{60}$$

$$(B_Q/Q)^2 = (B_V/V)^2 + (B_I/I)^2 \tag{61}$$

V and I are the voltage and current values, respectively.

For calculating the bias limit in R_{th} measurements, we suppose that the bias errors in the two temperature measurements are totally correlated. Note that, in this case, the last term on the right side of Eq. (59) would cancel the first and the second terms and then $B_{R\mathrm{th}}/R_{\mathrm{th}}$ would be equal to B_Q/Q.

Table 5 gives the different values used and calculated in our uncertainty estimation. The calculated value of $U_{R\mathrm{th}}/R_{\mathrm{th}}$ obtained in our data for different input heat fluxes are shown in Fig. 7. The highest uncertainty for R_{th} (up to 34%) occurs at lowest input power, and it decreases with an increase in the input power.

Table 5 Values considered for uncertainty estimation

Parameter	Value, %
P_U/U	2
P_I/I	2
B_U/U	2
B_I/I	2
P_Q/Q	2.8
B_Q/Q	2.8
$B_{R\mathrm{th}}/R_{\mathrm{th}}$	2.8

Experimental Results and Analysis

Figure 8a shows typical steady temperature profiles for the FMHP for operations from nearly 5 to approximately 37 W at a heat sink temperature of 35°C. Also shown for comparison is the steady-state temperature profile for a copper plate. The maximum temperature occurs in the region directly over the heater. The maximum evaporator temperature and temperature gradients for the FMHP are

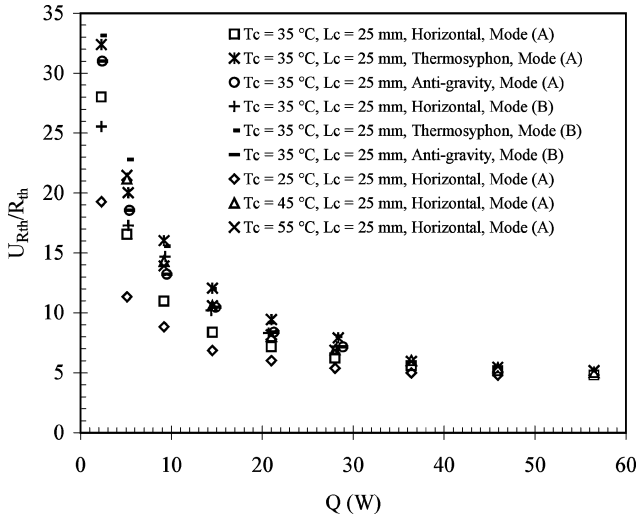

Fig. 7 Uncertainty of R_{th} vs Q for all experimental results.

considerably smaller than those obtained for the ungrooved copper plate. At an input power of 28.1 W, the maximum steady-state evaporator temperature for the FMHP is 65.4°C, whereas for the copper ungrooved plate the maximum evaporator temperature is 89.7°C. This results in a decrease in temperature gradients of approximately 24.3°C. As shown in Fig. 8a, the heat pipe operation reduces the slope of the temperature profile for the FMHP. This gives some indication of the ability of such FMHP to reduce the thermal gradients or localized hot spots.

Figure 9a shows the experimentally determined temperatures in the adiabatic section, T_{sat}, and at the evaporator, T_{ev}, and condenser, $T_c = 35$°C, end caps of the FMHP in a horizontal orientation. The adiabatic temperature T_{sat} is determined by calculating the average steady-state adiabatic temperatures, which are measured by the thermocouples located at 36.5, 56.5, and 76.5 mm from the end cap of the evaporator section (Fig. 8a). The temperature distribution trends are very similar for the other heat sink temperatures ($T_c = 45$ and 55°C) and are not shown here. Figure 9b shows the evaporator, the condenser, and the adiabatic thermal resistances computed from the measured temperatures and heat input data using the following definitions:

$$R_{\text{th}e} = (T_{\text{ev}} - T_{\text{sat}})/Q, \qquad R_{\text{th}c} = (T_{\text{sat}} - T_c)/Q$$
$$R_{\text{th}a} = \Delta T_{\text{sat}}/Q \tag{62}$$

where ΔT_{sat} is the saturation temperature variation in the adiabatic section.

The thermal resistance distributions shown in Fig. 9b show that the evaporator thermal resistance $R_{\text{th}e}$ decreases as the input power Q increases and then increases when the capillary limit is reached. Hence, the evaporator thermal resistance distribution trend allows for the experimental determination of the maximum capillary limit $Q_{\max}$. The condenser as well as the adiabatic thermal resistances decreases with increasing heat rate Q.

Figure 9c shows the source–sink temperature difference, $T_{\text{ev}} - T_c$, variations as a function of the input power Q, obtained for the FMHP and the copper ungrooved plate for $T_c = 35$°C. As shown, the source–sink temperature difference for the FMHP is significantly lower than that obtained for the copper ungrooved plate. The size of the source–sink temperature difference for the FMHP increases in direct proportion of the input heat flux rate and varies from almost zero at low-power levels (<1 W) to approximately 28°C at input power levels of approximately 28 W. Figure 9c again shows the effectiveness of the enhanced miniature heat pipe and clearly indicates the temperature reduction level that can be expected at higher heat flux rates before dryout.

The effective end cap to end cap thermal resistance of the FMHP is also given in Fig. 9c. Effective end cap to end cap thermal resistance R_{th} defined here as the overall end cap to end cap temperature drop

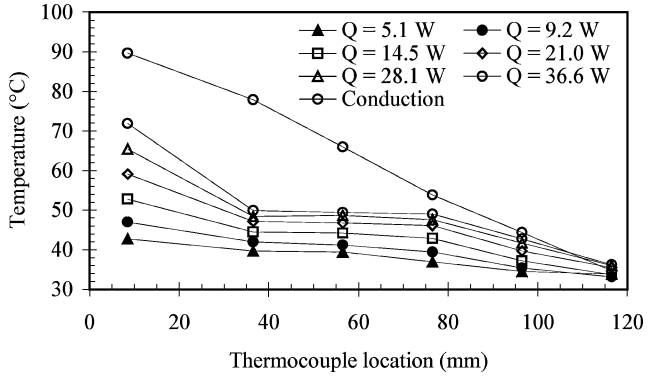

a) $T_c = 35$°C

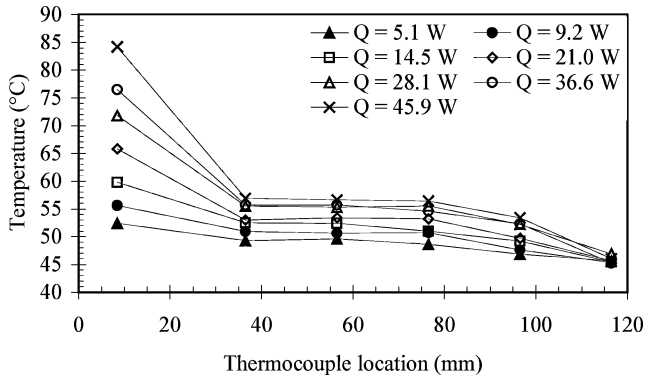

b) $T_c = 45$°C

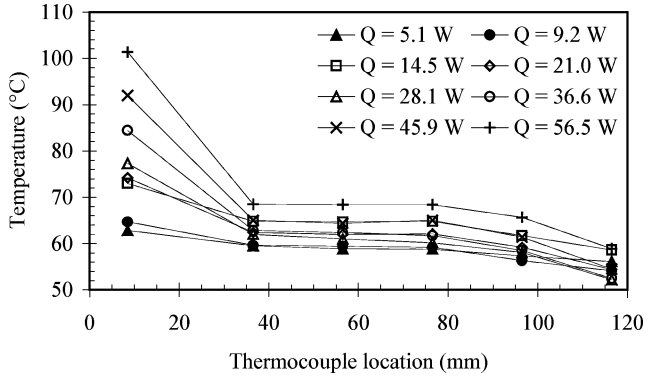

c) $T_c = 55$°C

Fig. 8 Axial temperature profile (horizontal position).

divided by the total applied heat load Q. A common characteristic of the thermal resistance presented is that the thermal resistance of the FMHP is high at low heat loads because a relatively thick liquid film resides in the evaporator. However, this thermal resistance decreases rapidly to its minimum value as the applied heat load is increased. Overall, the FMHP is found to have an approximate minimal thermal resistance of 1 K/W, whereas the ungrooved copper plate operates with a thermal resistance of 2 K/W. Note that the thermal resistance is a function of the heated and cooled surface areas in the evaporator and condenser sections, respectively, and is found to be dependent on the heat sink temperature.

Figure 10 shows the thermal resistance values of the FMHP obtained at four heat sink operating temperatures, $T_c = 25$, 35, 45 and 55°C, one operating temperature for each set of test points. These values allow for easy computation of the temperature drop from evaporator to condenser end cap. As shown, for a given heat sink temperature the thermal resistance of the miniature heat pipe decreases rapidly with respect to the input heat flux and asymptotically approaches a constant value. Also notice that for a given heat flux rate the thermal resistance decreases as the heat sink temperature increases.

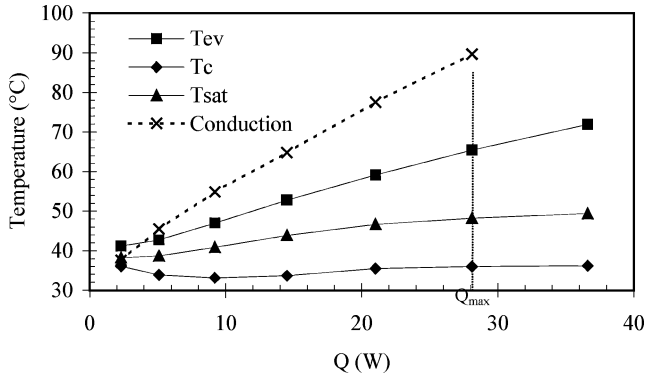

a) T_{ev}, T_c, and T_{sat} variations vs Q

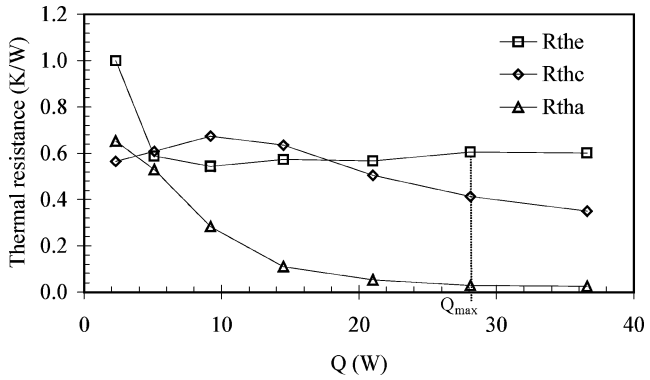

b) R_{the}, R_{thc}, and R_{tha} variations vs Q

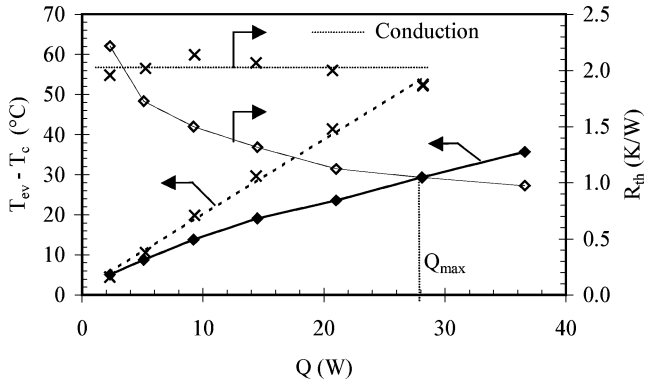

c) $T_{ev} - T_c$ and R_{th} variations vs Q

Fig. 9 FMHP thermal performance for $T_c = 35°C$ (horizontal position).

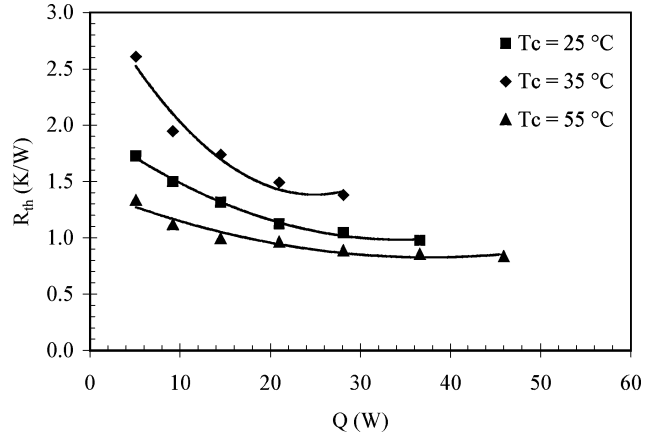

Fig. 10 Thermal resistance of the FMHP at various heat sink temperatures.

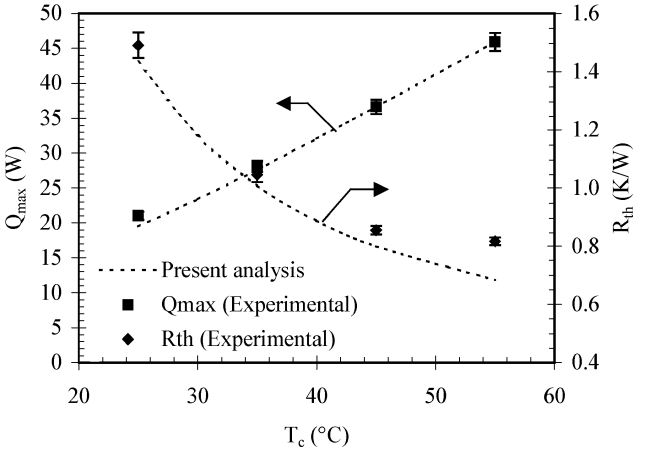

a) Q_{max} and R_{thf} vs Q

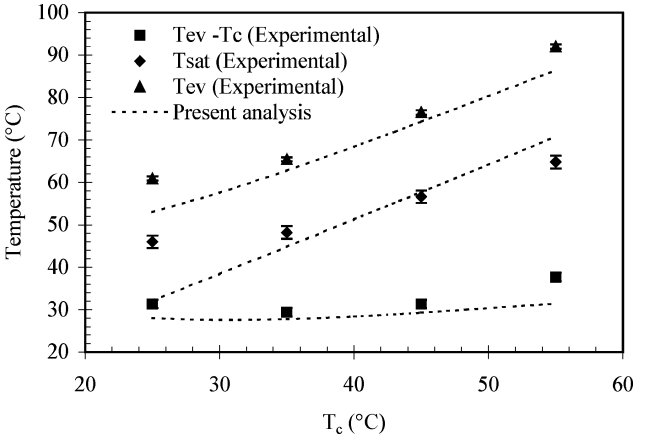

b) $T_{ev} - T_c$, T_{sat}, and T_{ev} vs Q

Fig. 11 Comparison between model and experimental data, $T_c = 35°C$, horizontal position.

The increase in Q_{max} with T_c is due to the decrease of the overall pressure drop ($\Delta P_l + \Delta P_v$). Indeed, when T_c increases, the vapor temperature T_{sat} increases, too (Fig. 9a). This results in a dramatic decrease of the vapor friction factor F_v [Eq. (28b)], and consequently, the vapor pressure drop ΔP_v decreases. However, the liquid pressure drop increases with T_c because of the augmentation of the liquid mass flow rate allowed by a decrease of the liquid friction factor F_l with T_c. Because the increase in ΔP_l is lower than the decrease in ΔP_v, the overall pressure drop ($\Delta P_l + \Delta P_v$) decreases.

The decrease of the FMHP thermal resistance is attributed mainly to the decrease of the evaporator thermal resistance when the heat flux increases. Indeed, increasing the heat flux leads to the enhancement of the evaporation process either in the grooves or in the mesh screen. The decrease of R_{th} is observed when the evaporation process is dominated by the capillary limit. However, for heat fluxes higher than the maximum capillary limit heat flux, intensified boiling process may occur in the capillary structure, and consequently, the evaporator thermal resistance increases. This results in an increase of the overall FMHP thermal resistance.

Figure 11a presents the experimental maximum heat flow rate Q_{max} and the minimum thermal resistance R_{thmin} of the FMHP oriented horizontally in the range of heat sink temperature of $T_c = 25$–$55°$ C. (The experimental data are indicated by symbols.) Q_{max} is defined to occur when the evaporator temperature and, hence, the end cap to end cap thermal resistance begin to rise sharply. The maximum heat rate increases from 21 W at $T_c = 25$–45.9 W at $T_c = 55°$ C. However, the minimum thermal resistance that corresponds to the capillary limit R_{thmin} decreases from 1.49 to 0.82 K/W when the heat sink temperature increases from 25 to 55°C. The dashed lines without symbols in Fig. 11a show the theoretical prediction results obtained with the geometrical characteristics listed in Table 4.

In these calculations, the meniscus contact angle θ_e is 35 deg. As shown, the model predicts the maximum capillary limit Q_{max} very well. The prediction of the minimum thermal resistance by the model fits quite well the experimental results. Overall, by taking into account the uncertainties in the experimental results and the hypotheses that are made in the theoretical calculations, we can conclude that the elaborated model is capable to predict well the experimental results. Figure 11b shows the experimental data and theoretical calculations for T_{ev}, T_{sat} and ΔT_{FMHP} in the range of $T_c = 25$–55° C.

To determine the significance of the gravitational forces, experiments are carried out with different FMHP orientations (Fig. 12a): horizontal position, thermosyphon position, and antigravity position. The heat sink temperature is fixed at $T_c = 40$°C. For heat rates $Q < 10$ W, the source–sink temperature differences are nearly the same for the different positions. However, for heat rates $Q > 10$ W, the FMHP becomes sensitive to the orientation. The antigravity position exhibits the highest source–sink temperature difference, whereas the thermosyphon position exhibits the lowest one.

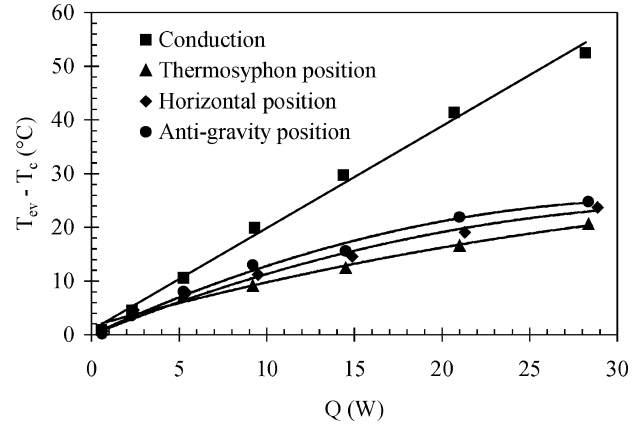

a) $T_{ev} - T_c$ variations vs heat rate Q

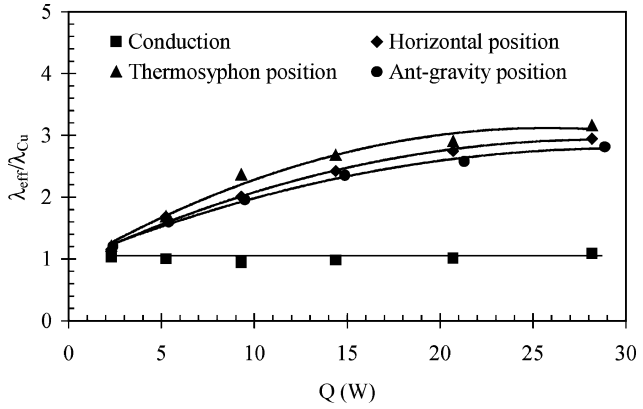

b) Effective thermal conductivity enhancement variations as function of Q, $\lambda_{Cu} = 380$ W/m · K

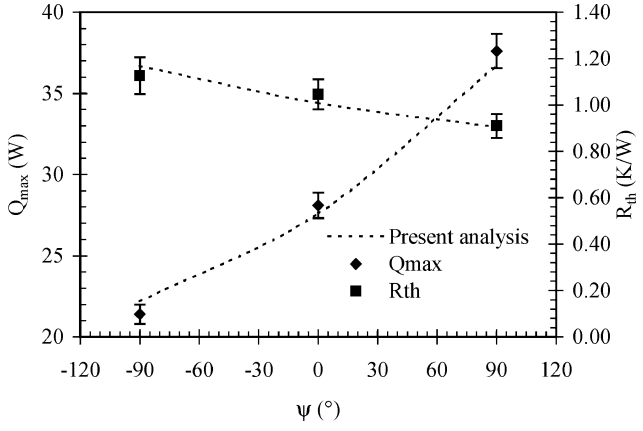

c) Comparison between model and experimental data

Fig. 12 Effect of FMHP orientation.

To quantify the experimental results better, additional data are taken from which an effective FMHP conductivity λ_{eff} could be calculated using Fourier's law. The axial heat rate, that is, the heat transported through the FMHP in the direction of the grooves, is computed by dividing the input power by the FMHP cross-sectional area. This value is then divided by the source–sink temperature difference. The obtained result is then multiplied by the linear distance between the points at which the source and sink temperatures are measured. As shown in Fig. 12b, the effective thermal conductivity variations of the copper ungrooved plate results in a nearly constant value for the effective thermal conductivity of 380 W/m · K. This value corresponds quite well (experimental uncertainties and heat losses) with the copper thermal conductivity data available in the open literature. The increasing trend observed in the effective thermal conductivity of the FMHP results from the decreasing temperature gradient occurring at high heat flux rates, which makes the heat pipes perform more effectively. The increased effective thermal conductivity of the FMHP amounts to an increase of nearly 300% for an input heat flux rate of about 28 W (Fig. 12b).

Figure 12c presents the experimental maximum heat flow rate of the FMHP in various orientations over the heat sink temperature $T_c = 35$°C. Maximum heat rate obtained in the horizontal orientation is found to be $Q_{max} = 28.1$ W with a heat load applied to mesh screen side. In the thermosyphon orientation, the maximum heat rate is $Q_{max} = 34.2$ W, whereas in the antigravity position the maximum capillary limit is found to be 21.4 W. Theoretical prediction results for the maximum heat rate and thermal resistance in the different orientations are also presented by the dashed lines based on different meniscus contact angles θ_e: For the horizontal orientation, $\theta_e = 35$ deg; for the antigravity position, $\theta_e = 10$ deg; and for the thermosyphon position $\theta_e = 100$ deg. Thus, the meniscus contact angle depends on the orientation of the FMHP. The meniscus contact angle for the antigravity position is lower than that of the thermosyphon position. This is caused by the liquid pooling effects. Indeed, for the antigravity position, there is a lack of liquid in the meshes and the meniscus recedes causing a decrease in the contact angle value. However, for the thermosyphon position, the meshes are filled with liquid and the contact angle value is higher than that obtained for the former orientation. The earlier mentioned values of θ_e are calculated from photographic-based experiments on the determination of the meniscus contact angles for water meshes in various orientations. The experimental data are well predicted by the present analysis. The predictive results indicate that an increase in the meniscus contact angle increases the maximum heat flow rate. The question of contact angle effects on maximum heat rate should be further investigated for FMHPs.

To study the effect of the heat flux distribution in the FMHP wall, experiments are carried out either with the heater placed on the machined side (heating downward) or on the cover plate side (heating upward) as shown in Fig. 13. The source–sink temperature difference variations as a function of the heat flux rate are shown in Figs. 14a and 14b for both cases of heating and for two FMHP orientations (horizontal and vertical positions). As shown in Fig. 14b, heating the cover side or the grooved side hardly affects the FMHP

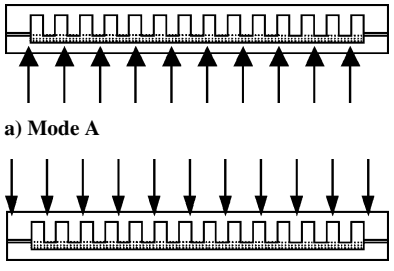

a) Mode A

b) Mode B

Fig. 13 Heating modes.

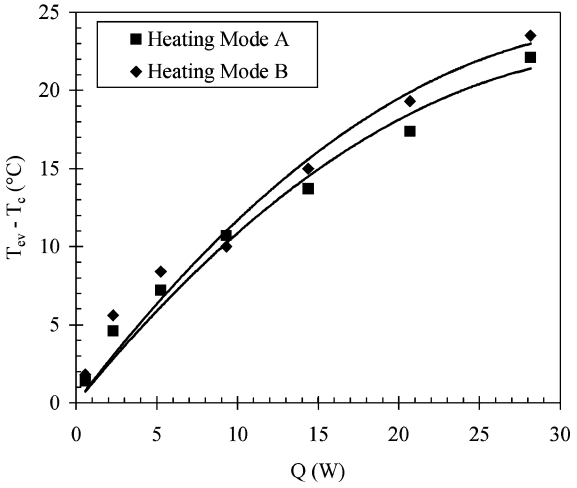

a) Horizontal position

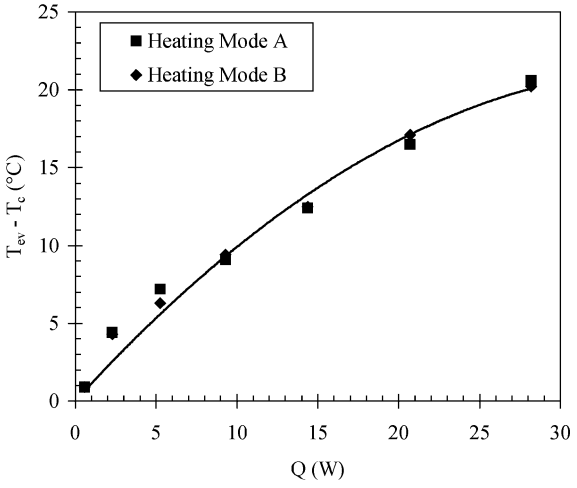

b) Thermosyphon position

Fig. 14 Effect of the heating modes.

thermal performance if the FMHP is vertically oriented. When the FMHP is oriented horizontally (Fig. 14a), heating the grooved side gives source–sink temperature difference higher than that obtained for the cover side heating case. However, the maximum gap of the source–sink temperature difference measured for the two heating modes is about 2°C, and this value is not large enough to make a difference between heating modes. Hence, it can be stated that there are not heating mode effects on the FMHP performance.

Conclusions

A combined experimental and analytical study is realized to determine the potential advantages of a mixed capillary structure. Experiments are conducted to verify the FMHP concept and determine the potential advantages of constructing arrays of rectangular microchannels as an integrated part of the high integrated electronic packages.

In the theoretical study, a model is developed to predict the thermal performance of FMHP including mixed capillary structure, rectangular grooves, and screen mesh. The model, which is based on the capillary flow and thermal resistance analysis, is able to predict the maximum capillary limit $Q_{\max}$ of the FMHP and its corresponding thermal resistance in various conditions. The effect of parameters such as the condenser temperature and the FMHP orientation is particularly studied. The maximum heat transport capacity increases with increases in condenser temperature; however, the FMHP thermal resistance decreases. The analytical results show that the FMHP thermal is affected by gravity. Indeed, the maximum capillary limit increases when the FMHP orientation is varied from the antigravity position to the thermosyphon one; however, the thermal resistance decreases.

In the experimental study, copper FMHP are machined, sealed, and filled with water as working fluid. The temperature measurements allow for a determination of the temperature gradients and maximum localized temperatures for the FMHPs. A technique is used to compare the copper MHP thermal performance to a copper plate having the same dimensions. In this way, the magnitude of the thermal enhancement resulting from the FMHPs could be determined. The thermal measurements show significantly reduced temperature gradients and maximum temperature decrease when compared to those of a copper plate having the same dimensions. Reductions in the source–sink temperature difference of 30°C and increases in the effective thermal conductivity of approximately 300% are measured for input power levels up to 30 W (horizontal position). Moreover, there is no heating mode effects on the enhanced FMHP thermal performance. However, the condenser temperature affects the FMHP thermal performance as predicted by the analytical results.

Although several issues are not addressed, such as the effect of the FMHP size, the effect of the fill charge, and the effect of screen size and/or performance degradation with respect to time, it is clear from these results that incorporating such FMHPs as part of highly integrated electronic packages can significantly improve the performance and reliability of electronic devices, by increasing the effective thermal conductivity, decreasing the temperature gradients, and reducing the intensity and the number of localized hot spots.

References

[1]Zaghdoudi, M. C., and Sarno, C., "Investigation on the Effects of Body Force Environment on Flat Heat Pipes," *Journal of Thermophysics and Heat Transfer*, Vol. 15, No. 4, 2001, pp. 384–394.

[2]Tantolin, C., Godet, C., and Zaghdoudi, M. C., "Heat Pipe Thermal Behavior From Frozen Start-up," *41st International Power Conversion and Intelligent Motion*, edited by J. M. Peter and A. Rufer, ZM Communications GMBH, 2000, pp. 355–360.

[3]Murakami, M., Ogushi, T., Sakurai, Y., Masumoto, H., Furukawa, M., and Imai, R., "Heat Pipe Heat Sink," *6th International Heat Pipe Conference*, Begell House, London, 1987, pp. 257–261.

[4]Plesh, D., Bier, W., Seidel, D., and Schubert, K., "Miniature Heat Pipes for Heat Removal From Microelectronic Circuits," *Micromechanical Sensors, Actuators, and Systems*, edited by D. Cho, R. Warrington Jr., et al., ASME-DCS-Vol. 32, American Society of Automotive Engineers, Fairfield, NJ, 1991, pp. 303–313.

[5]Sun, J.-Y., and Wang, C.-Y., "The Development of Flat Plat Heat Pipes For Electronic Cooling," *4th International Heat Pipe Symposium*, Japan Association for Heat Pipes, Tokyo, 1994, pp. 99–105.

[6]Ogushi, T., and Yamanaka, G., "Heat Transport Capability of Grooved Heat Pipes," *4th International Heat Pipe Symposium*, Japan Association for Heat Pipes, Tokyo, 1994, pp. 74–79.

[7]Cao, Y., Gao, M., Beam, J. E., and Donovan, B.,"Experiments and Analyses of Flat Miniature Heat Pipes," *Journal of Thermophysics and Heat Transfer*, Vol. 11, No. 2, 1997, pp. 158–164.

[8]Hopkins, R., Faghri, A., and Khtustalev, D.,"Flat Miniature Heat Pipes with Micro Capillary Grooves," *Journal of Heat Transfer*, Vol. 121, No. 1, 1999, pp. 102–109.

[9]Shimura, T., Nakamura, Y., Kawabata, K., Kimura, Y., and Niekawa, J., "Application of Aluminum Flat Heat Pipe For Close Chamber Cooling," *11th International Heat Pipe Conference*, Japan Association for Heat Pipes, Tokyo, 1999, pp. 148–153.

[10]Schneider, M., Yoshida, M., and Groll, M., "Investigation of Interconnected Mini Heat Pipe Arrays For Micro Electronics Cooling," *11th International Heat Pipe Conference*, Japan Association for Heat Pipes, Tokyo, 1999, p. 6.

[11]Schneider, M., Yoshida, M., and Groll, M., "Optical Investigation of Mini Heat Pipe Arrays With Sharp Angled Triangular Grooves," *Advances in Electronic Packaging*, EEP-Vol. 26-1 and 26-2, edited by D. Agonafer, M. Saka, and Y. C. Lee, American Society of Mechanical Engineers, Fairfield, NJ, 1999, pp. 1965–1969.

[12]Schneider, M., Yoshida, M., and Groll, M., "Cooling of Electronic Components By Mini Heat Pipe Arrays," *15th National Heat and Mass Transfer Conference and 4th ISHMT/ASME Heat and Mass Transfer Conference*, Inst. of Armament Technology, Pune, India, 2000, p. 8.

[13]Zampino, M. A., and Kinzy Jones, W., "Embedded Miniature Heat Pipes in Ceramic Cofire Substrates," *Aerospace Power Systems Conference*, Society of Automotive Engineers, Warrendale, PA, 1999, pp. 29–34.

[14]Wang, Y., and Vafai, K., "An Experimental Investigation of The Thermal Performance of an Asymmetrical Flat Plate Heat Pipe," *International Journal of Heat and Mass Transfer*, Vol. 43, No. 15, 2000, pp. 2657–2668.
[15]Wang, Y. X., Ma, H. B., and Peterson, G. P., "Investigation of the Temperature Distribution on Radiator Fins With Micro Heat Pipes," *Journal of Thermophysics and Heat Transfer*, Vol. 15, No. 1, 2001, pp. 42–49.
[16]Cao, Y., and Gao, M., "Wickless Network Heat Pipes For High Heat Flux Spreading Applications," *International Journal of Heat and Mass Transfer*, Vol. 45, No. 12, 2002, pp. 2539–2547.
[17]Ponnappan, R., "Novel Groove-Shaped Screen-Wick Miniature Heat Pipe," *Journal of Thermophysics and Heat Transfer*, Vol. 16, No. 1, 2002, pp. 17–21.
[18]Lin, L., Ponnappan, R., and Leland, J., "High Performance Miniature Heat Pipe," *International Journal of Heat and Mass Transfer*, Vol. 45, No. 15, 2002, pp. 3131–3141.
[19]Wang, Y. X., and Peterson, G. P., "Analysis of Wire-Bonded Micro Heat Pipe Arrays," *Journal of Thermophysics and Heat Transfer*, Vol. 16, No. 3, 2002, pp. 346–355.
[20]Noda, H., and Kumagai, M., "Effect of Mesh Shape on Maximum Capillary Pressure of Plain Weave Screen," *11th International Heat Pipe Conference*, Japan Association for Heat Pipes, Tokyo, 1999, pp. 85–89.
[21]Chi, S.W., *Heat Pipe Theory and Practice*, McGraw–Hill, New York, 1976.
[22]Longtin, J. P., Badran, B., and Gerner, F. M., "A One-Dimensional Model of Micro Heat Pipe During Steady-State Operation," *Journal of Heat Transfer*, Vol. 116, No. 3, 1994, pp. 709–715.
[23]Shah, R. K., and Bhatti, M. S., "Laminar Convective Heat Transfer in Ducts," *Handbook of Single Phase Convective Heat Transfer*, edited by S. Kakac, R. K. Shah, and W. Aung, Wiley, New York, 1987, pp. 3.45–3.70.
[24]Schneider, G. E., and DeVos, R., "Nondimensional Analysis for the Heat Transport Capability of Axially-Grooved Heat Pipes Including Liquid/Vapor Interaction," AIAA Paper 80-0214, 1980.
[25]Khrustalev, D., and Faghri, A. "Thermal Analysis of a Micro Heat Pipe," *Journal of Heat Transfer*, Vol. 116, No. 1, 1994, pp. 189–198.
[26]Faghri, A. *Heat Pipe Science and Technology*", 1st ed., Taylor and Francis, Philadelphia, 1995, pp. 123–140.
[27]Marcus, B. D., "Theory and Design of Variable Conductance Heat Pipes," NASA CR-2018, April 1972.
[28]Ikeda, Y., "The Permeability of a Screen Wick," *6th International Heat Pipe Conference*, Begell House, London, 1987, pp. 229–234.
[29]Kozai, H., Imura, H., and Takashima, K., "The Effective Thermal Conductivity of Screen Wicks," *3rd International Heat Pipe Symposium*, Japan Association for Heat Pipes, Tokyo, 1989, pp. 104–109.
[30]Rohsenow, W. M., and Clark, J. A., "Heat Transfer and Pressure Drop Data for High Heat Flux Densities to Water at High Sub-critical Pressures," Heat Transfer and Fluid Mechanics Inst., Stanford Univ. Press, Stanford, CA, 1951, pp. 193–207.
[31]Peterson, G. P., *An Introduction to Heat Pipes: Modeling, Testing and Applications*, 1st ed, Wiley, New York, 1994, pp. 68–70.
[32]Kline, S. J., and McClintock, F. A.,"The Description of Uncertainties in Single Sample Experiments," *Mechanical Engineering*, ASME Vol. 75, American Society of Mechanical Engineers, Fairfield, NJ, 1953, pp. 3–8.